

UC San Diego

UC San Diego Previously Published Works

Title

Electrochemistry in the Large Tunnels of Lithium Postspinel Compounds

Permalink

<https://escholarship.org/uc/item/6v98f67j>

Journal

Chemistry of Materials, 36(9)

ISSN

0897-4756

Authors

Hancock, Justin C

Ding, Patrick P

Choi, Yunyeong

et al.

Publication Date

2024-05-14

DOI

10.1021/acs.chemmater.4c00389

Supplemental Material

<https://escholarship.org/uc/item/6v98f67j#supplemental>

Copyright Information

This work is made available under the terms of a Creative Commons Attribution License, available at <https://creativecommons.org/licenses/by/4.0/>

Peer reviewed

Electrochemistry in the Large Tunnels of Lithium Post-spinel Compounds

Justin C. Hancock^{1,2}, Patrick Ding^{1,2}, Yunyeong Choi^{2,3}, Gerbrand Ceder^{2,3,4}, John T. Vaughey,^{2,5} Kent J. Griffith^{1,2,6,7*}, and Kenneth R. Poeppelmeier^{1,2,*}

¹Department of Chemistry, Northwestern University, Evanston, Illinois 60208, USA

²Joint Center for Energy Storage Research, Argonne National Laboratory, Argonne, Illinois 60439, USA

³Department of Materials Science and Engineering, University of California, Berkeley, California 94720, USA

⁴Materials Sciences Division, Lawrence Berkeley National Laboratory, Berkeley, California 94720 USA

⁵Chemical Sciences and Engineering Division, Argonne National Laboratory, Lemont, Illinois 60439, USA

⁶Department of Chemistry and Biochemistry, University of California, San Diego, California 92093, USA

⁷Program in Materials Science and Engineering, University of California, San Diego, California 92093, USA

*Corresponding authors: k3griffith@ucsd.edu, krp@northwestern.edu

Abstract

Lithium spinels ($\text{LiMM}'\text{O}_4$) are an important class of mixed-cation materials that have found uses in batteries, catalysis, and optics. Post spinels are a series of related framework structures with the $\text{AMM}'\text{O}_4$ host composition that are formed with larger A -site cations, typically under high pressure. Post-spinels have one-dimensional tunnel structures with pores that are larger than those in spinel and triangular in cross section; but they are relatively unexplored as intercalation electrodes. While lithium post-spinels have been previously found to be thermodynamically stable only at high pressures, we have identified a synthetic pathway that produces the lithium-containing materials at ambient pressure using an ion exchange process from the corresponding sodium post-spinels. Here we report the synthesis and a survey of the electrochemical properties of ten new lithium CaFe_2O_4 -type post-spinel compounds where $M = \text{Mn}^{3+}$, V^{3+} , Cr^{3+} , Rh^{3+} , Fe^{2+} , Mg^{2+} , Co^{2+} and $M' = \text{Ti}^{4+}$ and/or Sn^{4+} . Although complete delithiation is not achieved during electrochemical cycling, many of the lithium post-spinels have substantial charge storage capacity in Li battery cells owing to the ability of the large framework tunnels to accommodate more than one lithium ion per formula unit. Multiple redox couples are accessed for LiMnSnO_4 , $\text{Li}_{0.96}\text{Mn}_{0.96}\text{Sn}_{1.04-x}\text{Ti}_x\text{O}_4$, $\text{Li}_{0.96}\text{V}_{0.96}\text{Ti}_{1.04}\text{O}_4$, $\text{Li}_{0.96}\text{Cr}_{0.96}\text{Ti}_{1.04}\text{O}_4$, and $\text{LiFe}_{0.5}\text{Ti}_{1.5}\text{O}_4$. Compositions with moderate or poor lithium cyclability are also discussed for comparison. Redox mechanisms and trends are identified by comparing this new redox active framework to related spinels, ramsdellites, and 'Na_{0.44}MnO₂' structures, and from DFT electronic structures. *Operando* diffraction shows complex structural responses to lithium insertion and extraction in this post-spinel framework. A DFT framework was proposed to identify promising lithium post-spinel phases that could be accessed metastably under ambient pressure conditions and to assess their stability to lithium insertion and extraction. This work suggests that CaFe_2O_4 -type hosts are a promising new class of lithium-ion energy storage materials.

Introduction

Since reports of their electrochemical stability and activity in the mid-1980s, spinel compounds have received considerable attention as electrode materials for Li-ion batteries owing to their rate capability and high-voltage lattice stability.¹⁻³ LiMn_2O_4 and $\text{LiNi}_{0.5}\text{Mn}_{1.5}\text{O}_4$ and their derivatives have been studied in depth and have been used in commercial cells for their rate-enhancing attributes.^{1, 4-9} On the anode side, the spinel $\text{Li}[\text{Li}_{1/3}\text{Ti}_{5/3}]\text{O}_4$ ($\text{Li}_4\text{Ti}_5\text{O}_{12}$) has attracted significant attention as it has been identified as a ‘zero’ lattice expansion material with a volume change of just 0.2% upon lithiation to $\text{Li}_7\text{Ti}_5\text{O}_{12}$.¹⁰ This property has found uses in thin film devices, fixed volume applications, and end uses that requires extremely long life.^{2-3, 11-12} Beyond these famous examples, a vast range of other spinel compositions have been studied, including $\text{LiM}^{3+}\text{M}^{4+}\text{O}_4$ (e.g., LiCrTiO_4 , LiV_2O_4) and $\text{LiM}^{2+}\text{M}^{5+}\text{O}_4$ (e.g., LiNiVO_4).^{5, 13-19} The ordering of the filled octahedral sites in the spinel structure creates a three-dimensional network of intersecting channels, in which tetrahedral sites may be occupied by small cations such as Li^+ . This framework allows for facile ion diffusion and good electrochemical performance.^{1, 3} Furthermore, in spinels such as LiMn_2O_4 , lithium can either be extracted to form lithium vacancies ($\text{Li}_{1-x}\text{Mn}_2\text{O}_4$) or inserted to form spinel-ordered rock salt compositions (up to $\text{Li}_2\text{Mn}_2\text{O}_4$).¹ The latter process occurs exclusively in $\text{Li}_4\text{Ti}_5\text{O}_{12}$, forming $\text{Li}_7\text{Ti}_5\text{O}_{12}$ when fully lithiated.² Inclusion of cations with weak octahedral site preference (e.g. Fe^{3+}) into the spinel structure may result in inversion, resulting in highly charged, less mobile cations blocking the diffusion paths along these channels.^{18, 20}

In contrast to the well-studied spinel materials, there are comparatively few studies on post-spinel structures and they are primarily associated with the geological mantle.²¹⁻²⁵ The term post-spinel is used to refer to three phases that form when spinel is subjected to pressures on the order of 10 GPa: calcium ferrite (CF, CaFe_2O_4), marokite calcium manganate (CM, CaMn_2O_4), and calcium titanate (CT, CaTi_2O_4).²⁶⁻²⁸ Of these, the CF structure type is considered to be the most relevant in the field of ionics owing to its low activation barrier for alkali and alkaline-earth cation mobility.²⁹⁻³⁰ While the CF structure shares features that are common to other electrode materials, there are few lithium-ion battery studies due to the instability of the structure at ambient pressure and lack of viable synthetic pathways to the lithium analogues. Experimentally, CF versions of LiMn_2O_4 , LiFeTiO_4 , and LiRu_2O_4 have been studied as electrode materials for Li-ion batteries,³¹⁻³⁵ and $\text{Na}_{1-x}\text{V}_{1.25}\text{Ti}_{0.75}\text{O}_4$ and $\text{Li}_{1-x}\text{Mn}_2\text{O}_4$ have been studied as Mg battery cathodes.^{32, 36} Computational studies have identified various CaFe_2O_4 -structured hosts as promising cathode materials for Mg and Ca batteries.^{29, 37-39}

There are a limited number of CaFe_2O_4 -structured hosts known to be stable at ambient pressure.^{40, 41-42} However, we recently synthesized and reported that many previously unknown sodium post-spinel compounds are stable at ambient pressure.⁴³ Some lithium post-spinels have been synthesized at ambient pressure via ion exchange from a stable sodium post-spinel host lattice (e.g., LiFeTiO_4 and LiRu_2O_4),³³⁻³⁴ and we demonstrate here that the accessibility of metastable lithium post-spinel compounds under ambient pressures is a broad phenomenon. Because of the large size difference between Na^+ and transition metal cations Na/M antisite defects are expected to be negligible. This is analogous to the important work in ‘defect-free’ layered LiMnO_2 synthesized via ion exchange from NaMnO_2 in early layered-oxide cathode development.⁴⁴

Furthermore, while direct high-pressure synthesis of lithium post-spinels appears to result in Li/M antisite defects, soft synthesis via ion exchange of sodium post-spinels avoids formation of these defects.³² This work reports the synthesis and electrochemical Li⁺ insertion/disinsertion of ten new lithium post-spinels and builds upon the expanded phase space of sodium post-spinels to open a new family of prospective Li-ion battery cathode materials that can be accessed at ambient pressure.

Experimental

Synthesis of the sodium post-spinel starting materials. The sodium post-spinel phases were synthesized via high-temperature solid-state reactions as described previously.⁴³ Briefly, the starting materials were NaHCO₃ and the binary metal oxides for all syntheses except for NaFe_{0.5}Ti_{1.5}O₄ and NaV_{0.96}Ti_{1.04}O₄. Compounds susceptible to oxidation (those containing Fe²⁺, V³⁺, or Cr³⁺) were synthesized in a tube furnace under flowing Ar or 5% H₂ / 95% Ar. For NaFe_{0.5}Ti_{1.5}O₄, the reagents were Na₈Ti₅O₁₄ (synthesized by heating NaHCO₃ and TiO₂ in stoichiometric amounts at 900 °C for 24 hours), FeTiO₃ [Sigma] and TiO₂. Na_{0.96}V_{0.96}Ti_{1.04}O₄ was synthesized in two ways. In the first synthesis, NaHCO₃, VO₂, and TiO₂ were reacted under flowing 5% H₂ / 95% Ar at 700 °C for 12 hours, then 950 °C for 24 hours. In the second synthesis, Na₈Ti₅O₁₄, V₂O₃, and TiO₂ were reacted under flowing Ar at 950 °C for 24 hours. In subsequent sections, these two samples are referred to as LVT-H₂ and LVT-Ar, respectively.

All compounds, other than NaMnSnO₄, were quenched in air (if synthesis occurred in air) or cooled quickly by shutting off the power (if synthesis occurred in a tube furnace). NaMnSnO₄ was slowly cooled as described by Chiring *et al.*,⁴⁵ which likely explains why its composition is essentially the ideal, stoichiometric composition. The Na_{0.96}Mn_{0.96}Sn_{1.04-x}Ti_xO₄ compositions were quenched from 1100 °C as this was the temperature for which the extent of Ti⁴⁺ substitution is greatest.

Ion-exchange synthesis of lithium post-spinels. The lithium post-spinel compounds were synthesized via ion-exchange reactions. Mixtures of the sodium post-spinel and either LiNO₃ or a 2:3 mixture (by mole) of KCl and LiCl were placed in either alumina or platinum crucibles and heated above the melting point of LiNO₃ or the chloride eutectic. This was performed in air for all compositions except Na_{0.96}V_{0.96}Ti_{1.04}O₄ and NaFe_{0.5}Ti_{1.5}O₄, which were exchanged under flowing Ar. The temperature and time required for full exchange was composition dependent (see Results and Discussion section). Typically, ~12 grams LiNO₃ or the chloride mixture were used along with about 0.35 grams of sodium post-spinel. It is likely that this degree of excess of LiNO₃ or chloride mixture is not required, but a systematic variation of the ratios was not performed. Following the exchange reactions, the nitrates or chlorides were dissolved in water, and the Li post-spinels were separated using vacuum filtration. Note that other than hand grinding using an agate mortar and pestle, no attempt was made to control particle size and morphology.

X-ray characterization. Phase purity was assessed by laboratory powder X-ray diffraction (PXRD) using both Rigaku Ultima IV and Rigaku SmartLab X-ray diffractometers. These data were collected with Cu K α radiation over a 2θ range of 10–60° under ambient conditions. Rietveld refinement was performed using the General Structure Analysis System II (GSAS II) package.⁴⁶

Operando synchrotron X-ray diffraction measurements were carried out at Argonne National Laboratory on beamline 17BM-B. The samples were measured at ambient temperature in transmission geometry at 51 keV (0.24099 Å) with an area detector. All *operando* measurements were performed in the AMPIX cell, which has been described elsewhere.⁴⁷ Briefly, it contains a hard, conductive glassy carbon window to prevent inhomogeneous electrochemical reactions, which are a concern with flexible and/or non-conductive X-ray windows. Self-standing electrodes of $\text{Li}_{0.96}\text{Mn}_{0.96}\text{Sn}_{0.74}\text{Ti}_{0.30}\text{O}_4$ were fabricated with a 5:4:1 ratio of metal oxide/carbon black [Vulcan XC72R]/poly(tetrafluoroethylene) [PTFE, Sigma, 1 μm powder] uniaxially pressed into a pellet at 150 MPa. The active material loading of the 10-cm-diameter electrode was 13.5 mg cm⁻². AMPIX cells were constructed in an argon glovebox with lithium metal counter electrodes [Sigma, 99.9%], glass fiber separators [Whatman GF/B], and 1.0 M LiPF₆ dissolved in 1:1 v/v ethylene carbonate/dimethyl carbonate [EC/DMC, Sigma, battery grade]. The cell was cycled at a rate of C/3.5 corresponding to a current density of 0.46 mA cm⁻². Two-dimensional image data were converted to conventional one-dimensional diffraction patterns through integration in GSAS-II after calibration with LaB₆.⁴⁶ Background subtraction, primarily from the glassy carbon window, and normalization to X-ray intensity were performed on the one-dimensional integrated diffraction data.

Sequential Rietveld refinement of the unit cell parameters and metal positions from *operando* galvanostatic electrochemical (de)lithiation was performed in GSAS-II. The initial structure model was based on Rietveld refinement of the atomic coordinates, unit cell parameters, background, and instrument parameters (zero offset, *U*, *V*, and *W*) of the first *in situ* diffraction pattern prior to application of an applied current. For the sequential refinement, unit cell parameters, background coefficients, and metal *x* and *z* fractional coordinates were allowed to vary; refinement of the fractional atomic coordinates resulted in continuous variation of ±0.01 (Supporting Information). 2D diffraction images (integrated to 1D patterns) were recorded every 0.5 seconds and 20 subframes were summed to give 10 s time resolution, which corresponds to a Δ*x* of 0.0008 in $\text{Li}_{0.96-x}\text{Mn}_{0.96}\text{Sn}_{0.74}\text{Ti}_{0.30}\text{O}_4$ during each diffraction image collection.

Solid-state NMR spectroscopy. NMR spectra were recorded under magic angle spinning (MAS) in a static magnetic field of 9.4 T with a Bruker Avance III spectrometer. The samples were packed into 1.6-mm-diameter or 4.0-mm-diameter zirconia rotors and spectra were measured with Phoenix narrow-bore HX probes. *T*₁ (spin–lattice) relaxation was measured with a saturation-recovery pulse sequence for *T*₁ > 1 s or an inversion-recovery pulse sequence for *T*₁ < 1 s. All spectra were excited with a direct pulse–acquire pulse sequence using the following rf pulses: ⁷Li (1.6 mm – 75°, 2.4 μs, 104 kHz; 4 mm – 56°, 2.5 μs, 62.5 kHz); ⁶Li (4 mm – 90°, 1.6 μs, 156 kHz); and ²³Na (4 mm – 45°, 2 μs, 62.5 kHz). Recycle delays were ≥ 5*T*₁. The ^{6,7}Li and ²³Na chemical shifts were externally referenced to 1.0 M LiCl (aq. H₂O) at 0 ppm and solid NaCl at 7.2 ppm, respectively.

Coin cell construction and electrochemical measurements. Pristine ion-exchanged powders were thoroughly mixed with conductive carbon [Super P, AOT] using a mortar and pestle. This mixture was then added to and homogenized with a binder solution of polyvinylidene difluoride [PVDF, Kynar 1810] dissolved in 1-methyl-2-pyrrolidinone [Sigma, NMP, 99.5%, anhydrous].

The mass ratio of active material, conductive carbon, and PVDF was 8:1:1. The slurry was coated on aluminum foil then dried at 70 °C overnight in air. The area of the punched electrodes was 1.54 cm² with typical active mass loadings of 2–3 mg. Lithium metal foil [AOT, 99.9%] was used as the anode and separated from the cathode with a glass fiber separator [Whatman, GF/D] soaked with the electrolyte, 1.0 M LiPF₆ in 1:1 EC/DMC [Sigma, battery grade], which was used as received. The SS316 2032-size coin cells were electrochemically cycled in a multi-channel battery cycler (BCS-805, Bio-Logic) at room temperature. Theoretical capacities and C-rates were calculated based on complete Li removal from each composition.

Ab initio calculations. Density functional theory (DFT) was used as implemented in the Vienna Ab initio Simulation Package (VASP) using the projector augmented-wave method⁴⁸⁻⁴⁹ and the generalized gradient approximation as formulated by Perdew, Burke, and Ernzerhof.⁵⁰ For all stability calculations, the energy cutoff was set to 520 eV, and at least 1000 k-points were used per reciprocal atom. For geometry optimization, energies were converged to 10⁻⁷ eV atom⁻¹ for electronic steps and forces were converged to 0.01 eV Å⁻¹ for ionic steps. The Hubbard U correction was used for the electronic states of transition metals. U parameters were chosen to be consistent with oxide materials within the Materials Project database,⁵¹ as reported by Jain et al.⁵²

The CF post-spinel supercell was chosen to have 32 oxygen ions for all calculations, and ionic positions, cell shape, and cell volume were relaxed during energy minimization. For determining Li configurations, the three lowest electrostatic energy configurations of octahedral metal cations in Li₁(M,M')O₄ were computed. For Li concentrations above and below unity, the transition metal ordering was maintained as for Li₁(M,M')O₄ post-spinels, and only the Li configurations were varied. Thermodynamic stability was determined using the convex hull method; the DFT energies of all competing phases in each Li-M-M'-O chemical space were taken from the Materials project database.

The climbing nudged elastic band (NEB) method was used to calculate Li hopping barrier energies.⁵³ Excluding the initial and final states, a total of seven intermediate images were used to generate a trajectory between different sites. For the NEB calculations, energies were converged to 10⁻⁵ eV for electronic steps and 0.03 eV Å⁻¹ for ionic steps.

The pymatgen library was used to set up and analyze all the calculations in this work.⁵⁴

Results and Discussion

Ambient-pressure lithium post-spinel oxides via molten-salt ion exchange. Lithium post-spinel compounds were synthesized from sodium post-spinel precursors by ion exchange in either molten lithium nitrate or the molten LiCl–KCl eutectic. Lithium nitrate, with its low melting point and single cationic species, is a convenient lithium-ion exchange medium for oxidatively stable compounds. The chloride mixture was used to synthesize compounds sensitive to oxidation, such as Fe²⁺-containing NaFe_{0.5}Ti_{1.5}O₄, or to avoid decomposition of the nitrate when temperatures above 400 °C were necessary for complete ion exchange.

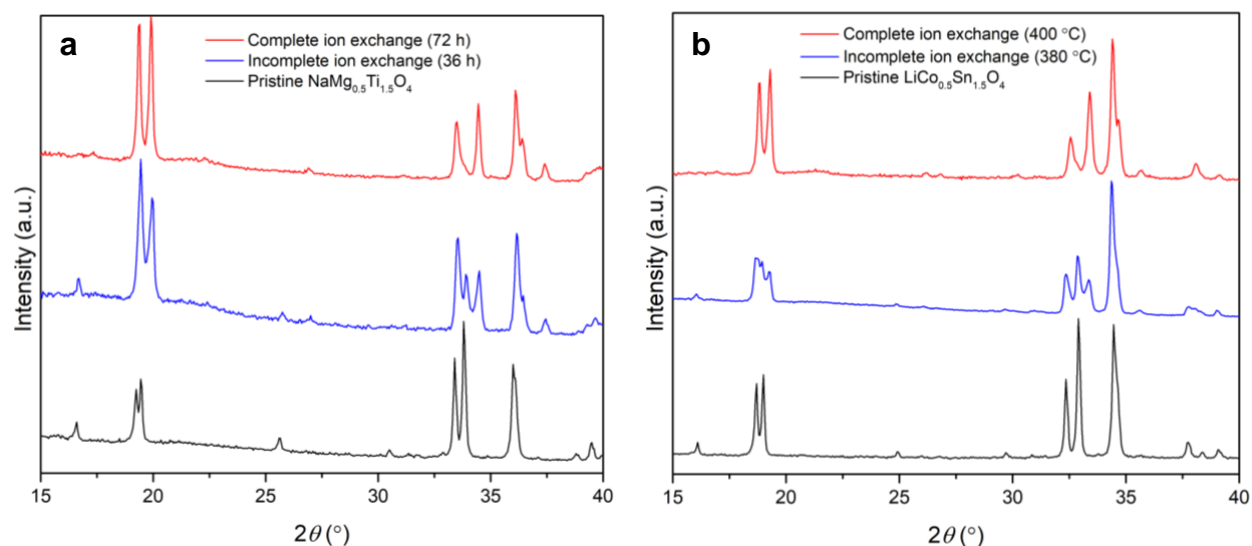


Figure 1 PXRD of a) pristine, partially Li-exchanged, and fully Li-exchanged NaMg_{0.5}Ti_{1.5}O₄ and b) pristine, partially Li-exchanged, and fully Li-exchanged NaCo_{0.5}Sn_{1.5}O₄. Note the growth and disappearance of peak intensity rather than shifting of peak positions, most obvious from 32–35° 2θ, indicative of a two-phase ion-exchange reaction mechanism.

The ion-exchange reactions appear to be two-phase processes (Figure 1). In every case for which incomplete ion exchange was observed, two sets of lattice parameters were observed: one corresponding to the sodium post-spinel precursor compound and the other to the fully exchanged lithium post-spinel product (*cf.* NMR section). No phases with intermediate lattice parameters were observed by PXRD. In all cases, powder X-ray diffraction showed only shifts in the lattice parameters within the *Pnma* space group of the sodium post-spinel precursors (and parent calcium ferrite structure) with no evidence for a change in symmetry or structure.

Li_{0.96}V_{0.96}Ti_{1.04}O₄ and LiFe_{0.5}Ti_{1.5}O₄ were successfully produced at 390 °C in one day in the chloride eutectic mixture (~40:1 mass ratio of alkali salt to sodium post-spinel). Owing to the susceptibility of V³⁺ and Fe²⁺ to oxidation, these reactions were carried out in a tube furnace with flowing Ar. The chloride eutectic melts at ~370 °C so 390 °C was the lowest and only temperature attempted for these ion exchange reactions.⁵⁵ Lower temperatures may be possible with a eutectic mixture such as KI/LiI or even via solid–solid ion exchange using solid LiI, but this possibility was not explored.

Ion exchange in molten LiNO_3 was carried out with an approximately 40:1 mass ratio of salt medium to sodium post-spinel and a heat treatment at 350 °C for two days.³³ For several of the compounds, ($\text{NaMg}_{0.5}\text{Ti}_{1.5}\text{O}_4$, $\text{NaCo}_{0.5}\text{Ti}_{1.5}\text{O}_4$, NaMnSnO_4 , and $\text{Li}_{0.96}\text{Mn}_{0.96}\text{Sn}_{1.04-x}\text{Ti}_x\text{O}_4$), these conditions proved to be sufficient for complete reaction. These conditions were insufficient for NaScTiO_4 , $\text{Na}_{0.96}\text{Cr}_{0.96}\text{Ti}_{1.04}\text{O}_4$, $\text{Na}_{0.96}\text{Rh}_{0.96}\text{Ti}_{1.04}\text{O}_4$, $\text{NaCo}_{0.5}\text{Sn}_{1.5}\text{O}_4$, and $\text{Na}_{0.96}\text{In}_{0.96}\text{Sn}_{1.04}\text{O}_4$ with partial to negligible ion exchange observed by PXRD in these cases.

For $\text{NaCo}_{0.5}\text{Sn}_{1.5}\text{O}_4$, the requirements for complete ion exchange were dependent on the synthesis conditions of the sodiated starting material. Two different samples were used for ion-exchange experiments, one synthesized at 1200 °C (48 hours, with an intermediate grinding and 10% excess NaHCO_3 added) and one synthesized at 1000°C (96 hours, with an intermediate grinding). The $\text{NaCo}_{0.5}\text{Sn}_{1.5}\text{O}_4$ synthesized at 1200 °C could be successfully ion exchanged using LiNO_3 at 400 °C, with intermediate temperatures (380 °C, 390 °C) resulting in only partial ion exchange. By contrast, the $\text{NaCo}_{0.5}\text{Sn}_{1.5}\text{O}_4$ synthesized at 1000 °C could be fully exchanged at 390 °C, even when heated for only 4 hours. One possible explanation for this would be that the lower synthesis temperature produced smaller particles. However, SEM shows that both samples have similar particle sizes (Figure S1). Another factor such as strain might influence the ion exchange process.

Neither $\text{Na}_{0.96}\text{Cr}_{0.96}\text{Ti}_{1.04}\text{O}_4$ nor $\text{Na}_{0.96}\text{Rh}_{0.96}\text{Ti}_{1.04}\text{O}_4$ completely exchanged at 400 °C, and it was clear from the yellow color of the solidified mixture after the reaction that oxidation of Cr^{3+} to Cr^{6+} occurs to some extent under these conditions. The chloride mixture was used thereafter. Heating at 450 °C for 36 hours in the chloride eutectic mixture resulted in complete exchange of $\text{Na}_{0.96}\text{Cr}_{0.96}\text{Ti}_{1.04}\text{O}_4$ and $\text{Na}_{0.96}\text{Rh}_{0.96}\text{Ti}_{1.04}\text{O}_4$. However, it should be noted that phase-pure $\text{Li}_{0.96}\text{Cr}_{0.96}\text{Ti}_{1.04}\text{O}_4$ could not be obtained using a platinum crucible. When the ion exchange of $\text{Na}_{0.96}\text{Cr}_{0.96}\text{Ti}_{1.04}\text{O}_4$ was carried out in a platinum crucible at 450 °C using the chloride eutectic, the solidified mixture was yellow after the reaction, suggesting the presence of Cr^{6+} . Furthermore, PXRD revealed the presence of platinum metal in the recovered product along with successfully exchanged $\text{Li}_{0.96}\text{Cr}_{0.96}\text{Ti}_{1.04}\text{O}_4$. These issues could be avoided by using an alumina crucible instead. In this case, the solidified chloride mixture was still white after the reaction, and phase pure $\text{Li}_{0.96}\text{Cr}_{0.96}\text{Ti}_{1.04}\text{O}_4$ was recovered.

NaScTiO_4 and $\text{Na}_{0.96}\text{In}_{0.96}\text{Sn}_{1.04}\text{O}_4$ did not fully exchange using these conditions, and degradation of $(\text{Na/Li})\text{ScTiO}_4$ was evident after the treatment. Given the previously published results for the exchange of NaMn_2O_4 , NaFeTiO_4 , and NaRu_2O_4 ,³¹⁻³⁴ and the results presented here, it would seem that larger framework cations (Sc^{3+} , In^{3+} , Sn^{4+}) suppress ion exchange, presumably by lowering the mobility of Na^+ . However, the higher temperatures required for the exchange of $\text{Na}_{0.96}\text{Cr}_{0.96}\text{Ti}_{1.04}\text{O}_4$ and $\text{Na}_{0.96}\text{Rh}_{0.96}\text{Ti}_{1.04}\text{O}_4$ do not follow this general trend. The authors suggest that the double-rutile frameworks for these compounds are less flexible because of the electronic configurations of Cr^{3+} and Rh^{6+} (d^3 and d^6 , respectively), both of which strongly prefer regular octahedra. This decrease in framework flexibility might kinetically hinder the ion-exchange process.

Rietveld refinement was performed for the new Li post-spinels. The lattice parameters and atom coordinates were refined, but U_{iso} variables were not refined owing to the data quality. The composition (ratio of alkali metal to transition metal) and symmetry were assumed to be conserved throughout the ion-exchange process. The lattice parameters for the new phases are presented in Table 1.

Table 1. Lattice parameters of new Li post-spinels synthesized via ion exchange from ambient-pressure sodium post-spinels.

Compound	<i>a</i> (Å)	<i>b</i> (Å)	<i>c</i> (Å)	<i>V</i> (Å ³)
Li _{0.96} V _{0.96} Ti _{1.04} O ₄	8.933(1)	2.9440(3)	10.664(1)	280.46(5)
Li _{0.96} Cr _{0.96} Ti _{1.04} O ₄	8.904(1)	2.9271(3)	10.628(1)	277.00(8)
LiMnSnO ₄	9.147(2)	3.0312(5)	10.942(2)	303.4(1)
Li _{0.96} Mn _{0.96} Sn _{0.74} Ti _{0.30} O ₄	9.099(2)	2.9955(5)	10.840(2)	295.5(2)
Li _{0.96} Mn _{0.96} Sn _{0.59} Ti _{0.45} O ₄	9.030(2)	2.9700(5)	10.813(2)	290.0(1)
Li _{0.96} Rh _{0.96} Ti _{1.04} O ₄	9.031(1)	2.9430(3)	10.641(1)	282.82(8)
LiCo _{0.5} Sn _{1.5} O ₄	9.237(1)	3.1297(3)	11.019(1)	318.54(8)
LiCo _{0.5} Ti _{1.5} O ₄	8.917(1)	2.9238(3)	10.642(1)	277.45(8)
LiFe _{0.5} Ti _{1.5} O ₄	8.941(1)	2.9526(4)	10.701(1)	282.50(9)
LiMg _{0.5} Ti _{1.5} O ₄	8.963(2)	2.9631(4)	10.727(2)	284.9(1)

Solid-state NMR spectroscopy. Magic-angle spinning (MAS) solid-state NMR spectra were recorded to examine the ion exchange process and resultant structures in further detail. One diamagnetic (LiMg_{0.5}Ti_{1.5}O₄) and one paramagnetic (LiMnSnO₄) compound were selected for NMR measurements.

In the case of LiMg_{0.5}Ti_{1.5}O₄, the ⁶Li and ⁷Li NMR spectra at 12.5 kHz MAS consist of a single isotropic resonance centered at 0.4 ± 0.1 ppm (Figure 2a) with a ⁶Li T_1 of 33 s and a ⁷Li T_1 of 2.3 s. The ⁷Li MAS spinning sideband manifold extends ~275 kHz (1770 ppm), arising from quadrupolar-broadened satellite transition intensity (Figure 2b). While broadening from heteronuclear dipolar coupling and chemical shift anisotropy are effectively eliminated by MAS for ⁷Li in this compound, homonuclear dipolar coupling is not. The ⁶Li isotropic resonance is narrower than that of ⁷Li owing to the smaller Larmor frequency and lower natural abundance of the former combining to yield weaker homonuclear dipolar coupling. As a check of the reaction completeness, ²³Na spectra were recorded on NaMg_{0.5}Ti_{1.5}O₄ before and after the ion exchange (Figure 2c). The LiMg_{0.5}Ti_{1.5}O₄ sample contained about 2.4% of the ²³Na signal of NaMg_{0.5}Ti_{1.5}O₄. At 25 kHz MAS, paramagnetic LiMnSnO₄ yields a ⁷Li MAS NMR pattern with two clear isotropic resonances, one centered at 750 ppm and the other at 0 ppm, with T_1 values of 4.8 ms and 8.9 ms, respectively, and large spinning sideband manifolds arising from anisotropic dipolar coupling between unpaired electrons and ⁷Li spins (Figure 3). At higher MAS rates, a third resonance with a T_1 of 3.9 ms and associated spinning sidebands appeared (Supplementary Figure S2). Although there is only one crystallographic sodium site in the calcium ferrite structure, multiple local

environments—as probed by NMR—are expected owing to different orderings of diamagnetic Sn and paramagnetic Mn^{3+} around the sodium center.

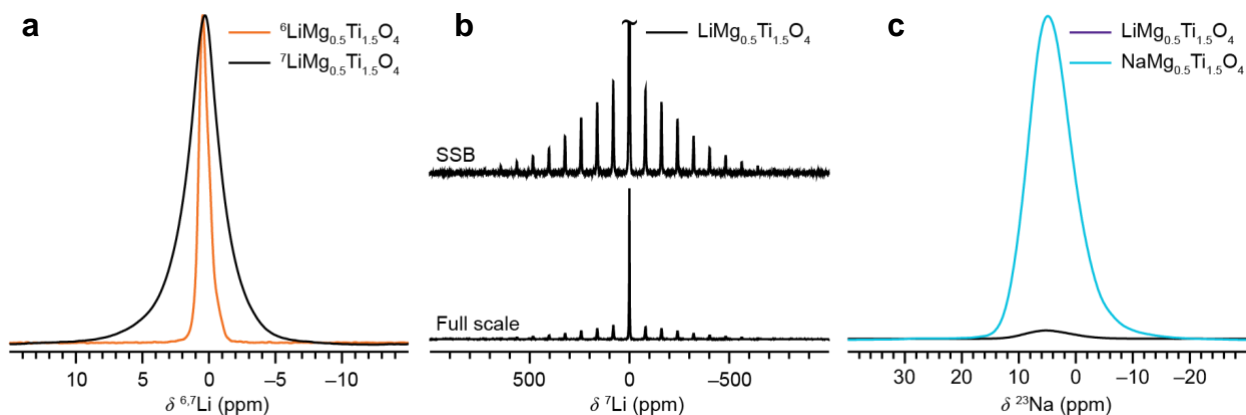


Figure 2 NMR spectra of $(\text{Na/Li})\text{Mg}_{0.5}\text{Ti}_{1.5}\text{O}_4$ at 12.5 kHz MAS and 9.4 T. (a) ${}^6\text{Li}$ and ${}^7\text{Li}$ centerband spectra of $\text{LiMg}_{0.5}\text{Ti}_{1.5}\text{O}_4$. (b) ${}^7\text{Li}$ spinning sideband manifold of $\text{LiMg}_{0.5}\text{Ti}_{1.5}\text{O}_4$ shown at full scale (bottom) and with the centerband intensity truncated (top). (c) ${}^{23}\text{Na}$ spectra of $\text{NaMg}_{0.5}\text{Ti}_{1.5}\text{O}_4$ and $\text{LiMg}_{0.5}\text{Ti}_{1.5}\text{O}_4$ showing residual 2.4% Na after Li-exchange. Spectra in (a) are scaled to equal maximum intensity. Spectra in (c) are normalized to the number of scans and moles of sample.

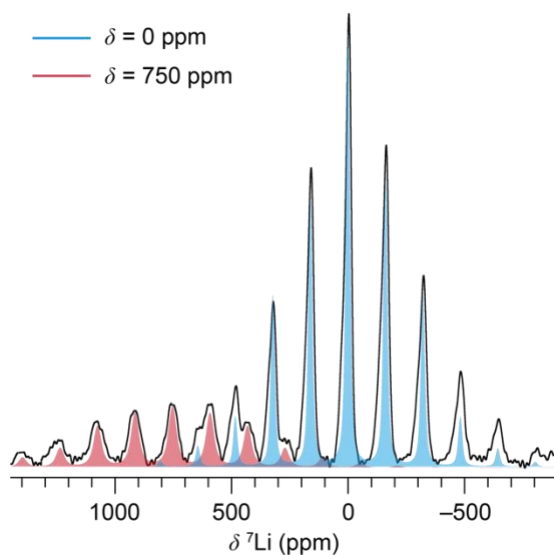


Figure 3 ${}^7\text{Li}$ NMR spectra of LiMnSnO_4 at 25 kHz MAS and 9.4 T. A two-component fit is shown with sub-spectra with isotropic shifts at 750 ppm and 0 ppm and large dipolar anisotropy. A third resonance and associated spinning sideband manifold appeared at higher MAS rates (Supplementary Figure S2) but the isotropic resonance could not be easily identified owing to strong peak overlap, temperature-dependent shift from variable frictional heating, and large anisotropy.

Initial electrochemistry

$\text{Li}_{0.96}\text{Mn}_{0.96}\text{Sn}_{1.04-x}\text{Ti}_x\text{O}_4$ ($x = 0, 0.3, 0.45$)

Lithium intercalation/deintercalation properties of electrode films of the ion-exchanged lithium post-spinel structures were examined in battery cells against lithium metal counter electrodes. On the initial charge of LiMnSnO_4 , a capacity of ~ 60 mAh/g is observed from 3.8 to 4.4 V (Figure 4a), compared to a theoretical capacity of 109 mAh/g for the removal of all lithium. This high-voltage process is reversible on the initial discharge, and an additional capacity is observed at lower voltages. A cutoff of 1.5 V results in a capacity of 120 mAh/g on the first discharge. A sloping profile suggests that the Li insertion occurs via a solid solution mechanism, though there are two broad peaks in the dQ/dV curve that are reminiscent of the subtle phase transitions in layered oxide cathodes. The tunnels appear to be able to accommodate more than one Li per formula unit, up to an approximate composition of $\text{Li}_{1.5}\text{MnSnO}_4$, and both the $\text{Mn}^{4+}/\text{Mn}^{3+}$ and $\text{Mn}^{3+}/\text{Mn}^{2+}$ redox couples are accessed. That the CaFe_2O_4 structure can accommodate more than one Li^+ per formula unit is consistent with the results published for CF- LiFeTiO_4 , which could be lithiated up to a composition of $\text{Li}_2\text{FeTiO}_4$.³³ Although the electrochemical processes for LiMnSnO_4 appear to be largely reversible, some capacity fade is observed; the capacity drops to ~ 100 mAh/g after 10 cycles.

Sn^{4+} can be substituted by Ti^{4+} in the $\text{Na}_{0.96}\text{Mn}_{0.96}\text{Sn}_{1.04-x}\text{Ti}_x\text{O}_4$ series to some extent, with x reaching up to ~ 0.45 at 1100 °C. Because these compositions must be quenched to avoid decomposition, the CF phase deviates from the ideal stoichiometry owing to Na^+ vacancies. The substitution has the effect of increasing the gravimetric capacity owing to the lower mass of Ti^{4+} relative to Sn^{4+} for the $\text{Li}_{0.96}\text{Mn}_{0.96}\text{Sn}_{0.74}\text{Ti}_{0.30}\text{O}_4$ composition, but further gains in capacity are not observed for $\text{Li}_{0.96}\text{Mn}_{0.96}\text{Sn}_{0.59}\text{Ti}_{0.45}\text{O}_4$. $\text{Li}_{0.96}\text{Mn}_{0.96}\text{Sn}_{0.74}\text{Ti}_{0.30}\text{O}_4$ and $\text{Li}_{0.96}\text{Mn}_{0.96}\text{Sn}_{0.59}\text{Ti}_{0.45}\text{O}_4$ have initial discharge capacities of 130–140 mAh/g and similar discharge capacities of ~ 120 mAh/g after 10 cycles (Figure 4c and e). Ti^{4+} substitution appears to enhance electrochemical reversibility. Approximately 19% of the capacity is lost between the first and 10th cycles for LiMnSnO_4 , whereas only about 8% is lost for $\text{Li}_{0.96}\text{Mn}_{0.96}\text{Sn}_{0.59}\text{Ti}_{0.45}\text{O}_4$.

Interestingly, polarization increases in the high voltage range (>3 V) for each of the three Li-Mn-Sn-Ti-O compositions. Voltage fade occurs on discharge during cycling; a peak in the dQ/dV plot is observed at about 3.8 V on discharge during the first cycle for each composition, which drops to 3.5–3.6 V by the 5th cycle (Figure 4b, 4d, and 4f). The corresponding peak in the charge curve increases in voltage by about 0.3 V.

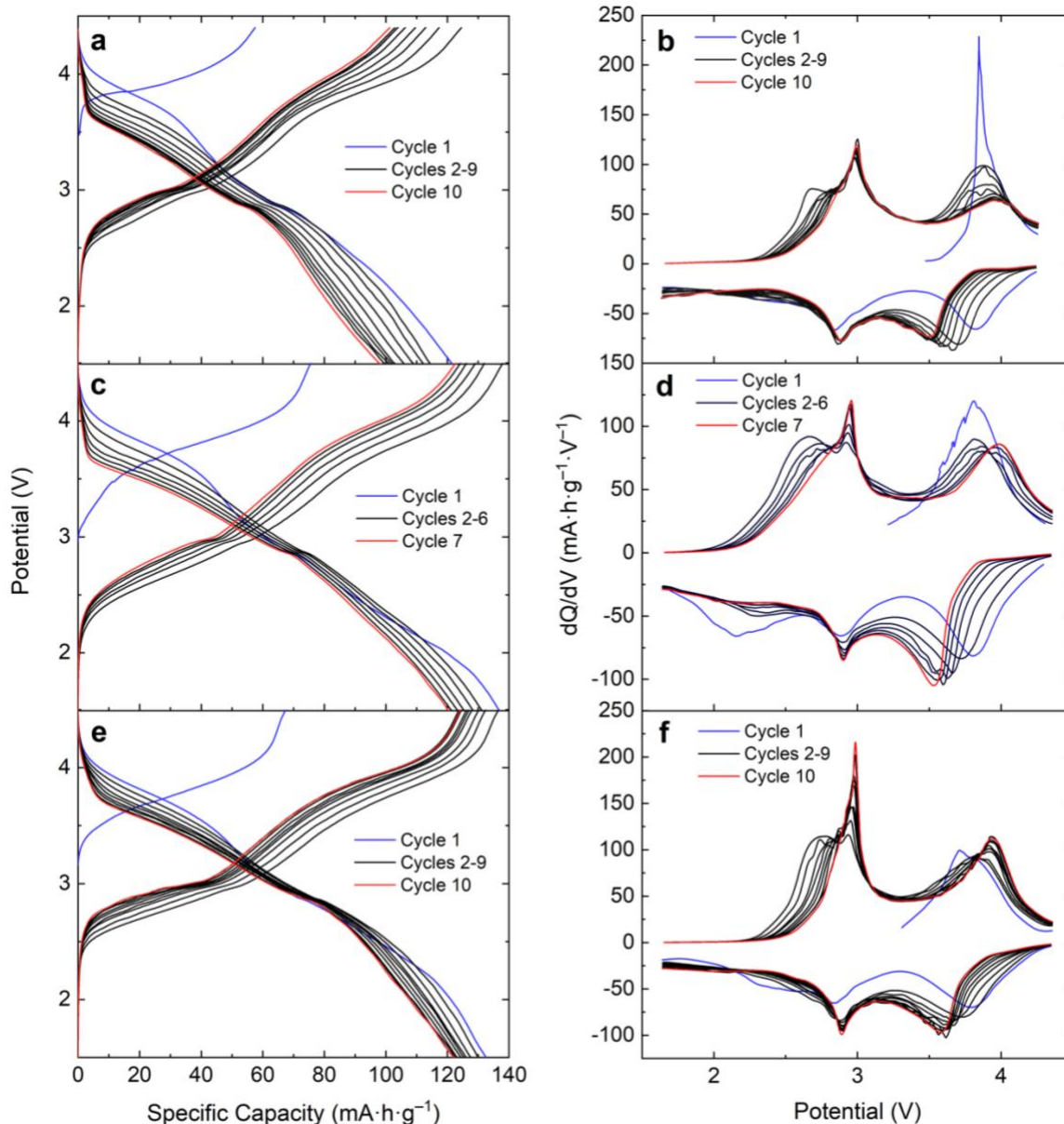


Figure 4 Galvanostatic cycling curves and dQ/dV curves for (a, b) LiMnSnO_4 , (c, d) $\text{Li}_{0.96}\text{Mn}_{0.96}\text{Sn}_{0.74}\text{Ti}_{0.30}\text{O}_4$, and (e, f) $\text{Li}_{0.96}\text{Mn}_{0.96}\text{Sn}_{0.59}\text{Ti}_{0.45}\text{O}_4$ cycled at $C/20$.

The electrochemical properties of the ramsdellite polymorph of LiMnSnO_4 (no spinel polymorph is known) have been investigated previously.⁵⁶ Compared to the CF polymorph, the ramsdellite polymorph has a higher initial charge capacity (~ 100 mAh/g), and a flatter voltage plateau. In addition, the voltage fade is lower in the ramsdellite polymorph. However, it should be noted that ramsdellite polymorph was synthesized via the urea-assisted combustion method resulting in a small particle size (~ 250 nm according to the Scherrer equation, but the scanning electron image suggests much smaller particles are present (< 100 nm)). By contrast, the CF- NaMnSnO_4 starting material in this study was synthesized via solid-state reaction at 1200 °C and then ion exchanged to form CF- LiMnSnO_4 . SEM reveals that the CF- LiMnSnO_4 particles vary in

size, but are micron-sized, up to ~10 μm for larger particles (Figure S1). Thus, some of the differences in the electrochemical behavior may result from differences in synthetic method and average crystallite size.

While the titanium end-member of the $\text{Na}_{0.96}\text{Mn}_{0.96}\text{Sn}_{1.04-x}\text{Ti}_x\text{O}_4$ series, CF- NaMnTiO_4 (thus also CF- LiMnTiO_4), cannot be synthesized at ambient pressure, two polymorphs of the composition LiMnTiO_4 (spinel and ‘ $\text{Na}_{0.44}\text{MnO}_2$ -type’, the latter synthesized via ion exchange of NaMnTiO_4 with the ‘ $\text{Na}_{0.44}\text{MnO}_2$ -type’ structure) are known, and their electrochemistry has been studied.^{5, 17, 57} Curiously, all four of these phases (CF- LiMnSnO_4 , CF- $\text{Li}_{0.96}\text{Mn}_{0.96}\text{Sn}_{1.04-x}\text{Ti}_x\text{O}_4$, spinel LiMnTiO_4 , and ‘ $\text{Na}_{0.44}\text{MnO}_2$ -type’ LiMnTiO_4) share the characteristic that only about half of the theoretical capacity is accessed on charging, i.e., none of the compositions can be fully delithiated, at least at room temperature. By contrast, the spinel, ‘ $\text{Na}_{0.44}\text{MnO}_2$ -type’, and CF polymorphs of LiMn_2O_4 can be essentially fully delithiated, though degradation of the framework occurs in the spinel phase at high degrees of Li extraction.^{6, 31, 57-58} Thus, Ti^{4+} or Sn^{4+} substitution for Mn^{4+} appears to decrease accessible charge capacity in all of these structure types despite no change in the nominal quantity of oxidizable Mn^{3+} .

$\text{Li}_{0.96}\text{V}_{0.96}\text{Ti}_{1.04}\text{O}_4$, $\text{LiFe}_{0.5}\text{Ti}_{1.5}\text{O}_4$, and $\text{Li}_{0.96}\text{Cr}_{0.96}\text{Ti}_{1.04}\text{O}_4$

$\text{Li}_{0.96}\text{V}_{0.96}\text{Ti}_{1.04}\text{O}_4$, $\text{Li}_{0.96}\text{Cr}_{0.96}\text{Ti}_{1.04}\text{O}_4$, and $\text{LiFe}_{0.5}\text{Ti}_{1.5}\text{O}_4$ share many similarities in their electrochemical behavior. With each compound, there is the possibility of accessing one redox couple at high voltage and a separate redox couple at a lower voltage: the $\text{V}^{4+/3+}$, $\text{Cr}^{4+/3+}$, and $\text{Fe}^{3+/2+}$ couples can be accessed during initial lithium extraction ($\text{Li}_{1-x}(\text{M},\text{Ti})_2\text{O}_4$) while the $\text{Ti}^{4+/3+}$ couple is active at lower voltages ($\text{Li}_{1+x}(\text{M},\text{Ti})_2\text{O}_4$). Experimentally, these processes are observed for all three compounds.

Two different samples of $\text{Li}_{0.96}\text{V}_{0.96}\text{Ti}_{1.04}\text{O}_4$ were prepared as described in the experimental section. For LVT- H_2 , the initial charge capacity is ~80 mAh/g, compared to the theoretical capacity of 152 mAh/g. On discharge, two plateaus are observed (Figure 5a). The first, which is the reverse of the process on the initial charge, occurs between 3.2 V and 2.6 V. The second process occurs at ~1.4 V (vs Li^+/Li) and has a shallower slope (sharper in dQ/dV). These two processes are assigned to the $\text{V}^{4+/3+}$ and $\text{Ti}^{4+/3+}$ redox couples, respectively. The capacity of the low-voltage process is greater than that of the high-voltage process, and the total discharge capacity is ~225 mAh/g during the first discharge, which suggests the approximate composition varies from $\text{Li}_{0.5}\text{V}_{0.96}\text{Ti}_{1.04}\text{O}_4$ to $\text{Li}_2\text{V}_{0.96}\text{Ti}_{1.04}\text{O}_4$. These processes are reversible on subsequent cycles, and a total capacity of over 200 mAh/g is maintained after 10 cycles. For LVT-Ar, the discharge capacity is smaller, 178 mAh/g by the tenth discharge (Figure 5c). The origin of the lower capacity for LVT-Ar compared to LVT- H_2 is unclear; it may be related to defects or surface chemistry but this requires further investigation. Minimal changes are observed in the dQ/dV plot, and the capacity actually increased slightly between the second and eleventh cycles.

The electrochemical behavior of $\text{LiFe}_{0.5}\text{Ti}_{1.5}\text{O}_4$ is similar to that of $\text{Li}_{0.96}\text{V}_{0.96}\text{Ti}_{1.04}\text{O}_4$, with two voltage plateaus observed during the initial discharge (Figure 5e). In contrast to $\text{Li}_{0.96}\text{V}_{0.96}\text{Ti}_{1.04}\text{O}_4$, the $\text{LiFe}_{0.5}\text{Ti}_{1.5}\text{O}_4$ electrode was discharged first. This was because during the washing step, it became clear the $\text{LiFe}_{0.5}\text{Ti}_{1.5}\text{O}_4$ was being oxidized by water. Gas bubbles,

presumably H_2 , formed on the initially black $\text{LiFe}_{0.5}\text{Ti}_{1.5}\text{O}_4$, and after filtering the material became a green-brown color. Thus, the material used to create the laminate was actually $\text{Li}_{1-x}\text{Fe}_{0.5}\text{Ti}_{1.5}\text{O}_4$. It may be possible to avoid this chemical oxidation with a milder salt removal step, *e.g.*, with alcohol. The voltage plateau corresponding to the $\text{Fe}^{3+/2+}$ redox couple is lower in

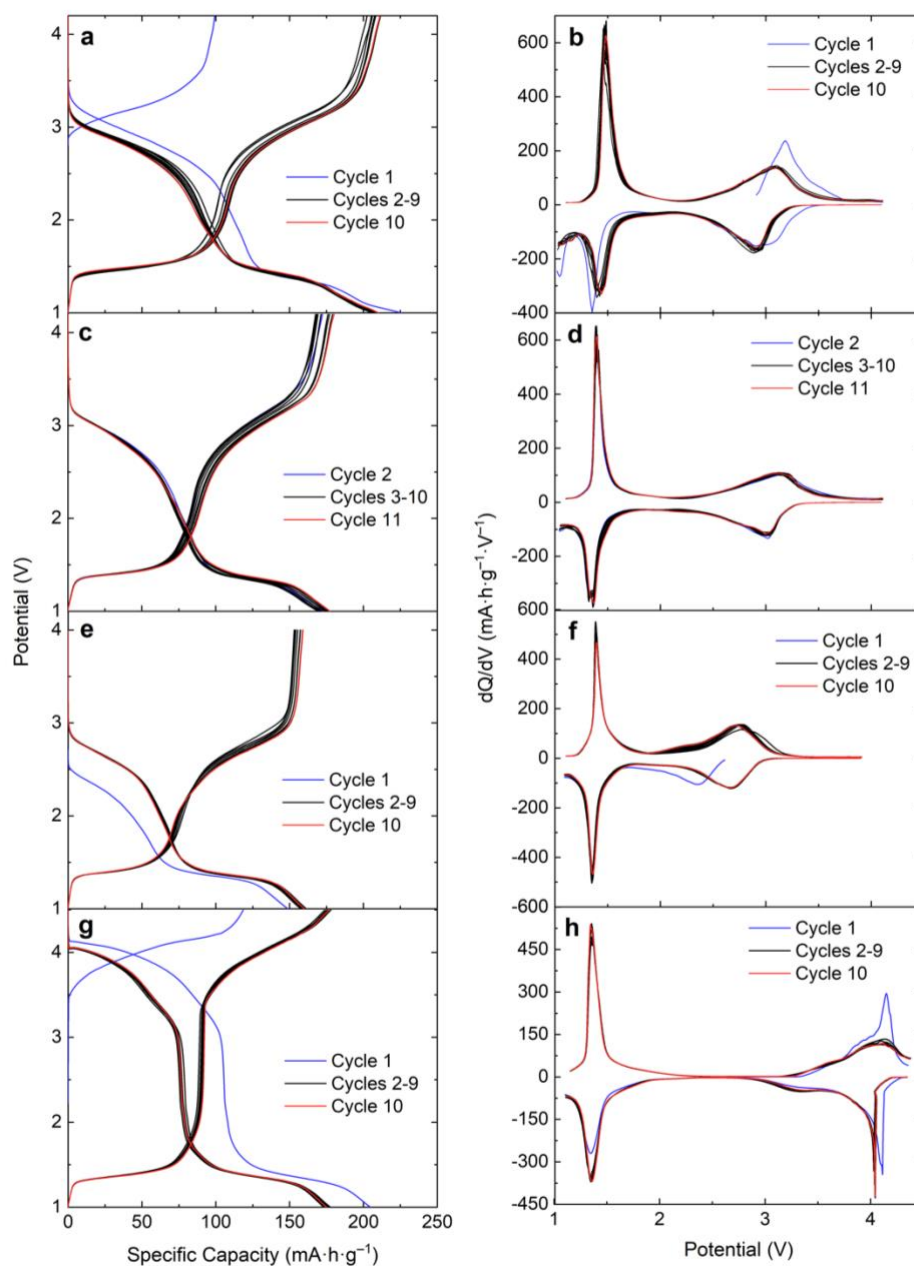


Figure 5 Galvanostatic cycling curves and dQ/dV curves for (a, b) LVT- H_2 , (c, d) LVT-Ar, (e, f) $\text{LiFe}_{0.5}\text{Ti}_{1.5}\text{O}_4$, and (g, h) $\text{Li}_{0.96}\text{Cr}_{0.96}\text{Ti}_{1.04}\text{O}_4$ cycled at $C/20$. Cycle 1 is not shown for LVT-Ar because of voltage instability resulting in artificially high capacity during the first cycle.

voltage than the $V^{4+/3+}$ couple by about 0.2 V and the capacity is similar, suggesting the charged material reaches a composition of approximately $Li_{0.5}Fe_{0.5}Ti_{1.5}O_4$. Because iron is not expected to be oxidized to the Fe^{4+} oxidation state with an upper cutoff voltage of 3.5 V, this means that the full theoretical capacity for the $Fe^{3+/2+}$ redox couple is nearly accessed. On discharge, the approximate composition of $Li_{1.5}Fe_{0.5}Ti_{1.5}O_4$ is reached, with the capacity reaching 160 mAh/g on the tenth cycle.

The initial charge capacity of $Li_{0.96}Cr_{0.96}Ti_{1.04}O_4$ is the highest among all the CF compounds tested, reaching a capacity of ~ 120 mAh/g (upper cutoff voltage = 4.5 V). Li extraction occurs primarily from 3.75–4.25 V. This process appears to be mostly reversible on discharge, and, as with $Li_{0.96}V_{0.96}Ti_{1.04}O_4$ and $LiFe_{0.5}Ti_{1.5}O_4$, a low voltage plateau is also present at ~ 1.4 V (Figure 5g). While the low-voltage process shows very little capacity fade, the high-voltage process associated with the $Cr^{4+/3+}$ redox couple is accompanied by capacity fade between the first and second cycles, after which stable cycling is observed with minimal capacity loss. The discharge capacity of the high-voltage process during the second cycle is ~ 75 mAh/g, which is about half of the theoretical capacity. The total capacity of the tenth discharge is ~ 175 mAh/g. Although there is large capacity fade between the first and second cycles in the high voltage region, this does not seem to be associated with any decomposition of the $Li_{0.96}Cr_{0.96}Ti_{1.04}O_4$ electrode. *Ex situ* PXRD reveals that the CF structure is well-maintained after 10 cycles (Figure 6). As with LVT-H₂, some voltage fade is observed on discharge between the first and second cycles, with little change between cycles 2–

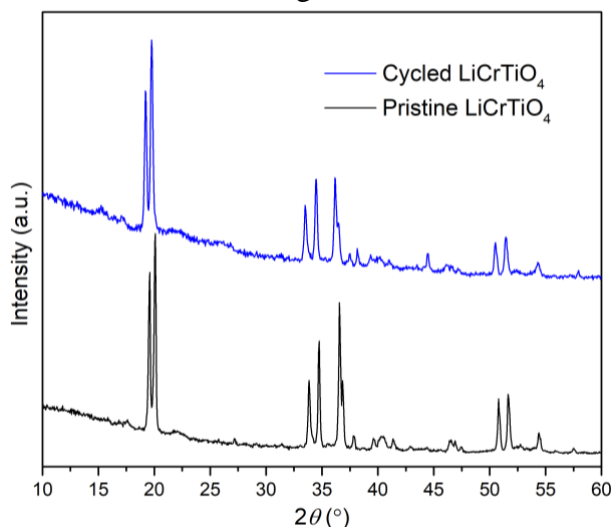


Figure 6 PXRD of pristine $Li_{0.96}Cr_{0.96}Ti_{1.04}O_4$ powder and an electrode of $Li_{0.96}Cr_{0.96}Ti_{1.04}O_4$ cycled 10 times between 1.0 V and 4.5 V and ending on a charge cycle.

the degree to which lithium can be extracted. However, it should be pointed out that the full theoretical capacity for the ‘ $Na_{0.44}MnO_2$ -type’ polymorph of $LiMnTiO_4$ was reached successfully by cycling at high temperature (60 °C).⁵⁷ Perhaps similar behavior could be observed for the other previously mentioned phases. In contrast to spinel $LiVTiO_4$, no reversible capacity at high voltages was reported for spinel $LiCrTiO_4$. While a voltage plateau is observed on charging to 5 V, no high-

10 (Figure 5h).

To the best of our knowledge, no other polymorphs of $LiFe_{0.5}Ti_{1.5}O_4$ have been studied electrochemically. However, there are known spinel and ramsdellite polymorphs for both $LiVTiO_4$ and $LiCrTiO_4$ for which electrochemical studies have been published.^{14-15, 59-60} The $V^{4+/3+}$ redox couple can be accessed for both the spinel and ramsdellite polymorphs, but the capacity is limited to ~ 90 mAh/g and ~ 60 mAh/g, respectively, which is strikingly similar to the behavior of CF- $Li_{0.96}V_{0.96}Ti_{1.04}O_4$ on the initial charge. These results, combined with the results in the manganese compounds, suggest that there is something intrinsic about the composition of these phases rather than the structure that suppresses the degree to which the high-voltage redox couples can be accessed and

voltage plateau is observed on discharge. Thus, the $\text{Cr}^{4+/3+}$ redox couple seems to be inaccessible for the spinel polymorph. However, $\text{Cr}^{4+/3+}$ redox, or possibly even Cr^{6+} , appears to be accessible for both the CF and ramsdellite polymorphs, although in neither case is the full theoretical capacity reached. On the other hand, the low-voltage behavior is quite similar for the spinel and ramsdellite phases for both LiVTiO_4 and LiCrTiO_4 . In each case, additional lithium can be inserted and the $\text{Ti}^{4+/3+}$ redox couple can be accessed around 1.5 V. The full theoretical capacity was reached for each polymorph, although LiCrTiO_4 required low current density conditions to access the full capacity. The $\text{Ti}^{4+/3+}$ redox couple for the CF phases can also be accessed at similar voltages. However, full capacity was only observed for LVT-H₂, while only about half of the theoretical capacity was accessed for other samples (LVT-Ar, $\text{Li}_{0.96}\text{Cr}_{0.96}\text{Ti}_{1.04}\text{O}_4$, and $\text{LiFe}_{0.5}\text{Ti}_{1.5}\text{O}_4$).

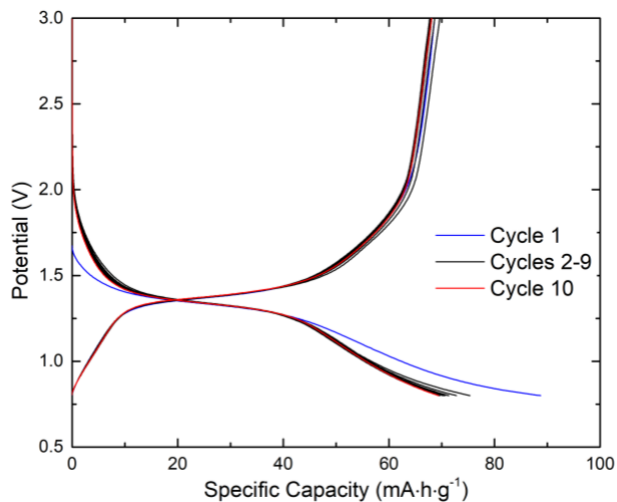


Figure 7 Galvanostatic cycling curves for $\text{LiMg}_{0.5}\text{Ti}_{1.5}\text{O}_4$ cycled at $C/20$.

$\text{LiMg}_{0.5}\text{Ti}_{1.5}\text{O}_4$

While all metal cations are in their highest oxidation states in $\text{LiMg}_{0.5}\text{Ti}_{1.5}\text{O}_4$ and Li cannot be extracted (at least without oxygen redox), the results for the preceding compounds suggested that $\text{LiMg}_{0.5}\text{Ti}_{1.5}\text{O}_4$ may still accommodate additional Li and act as an anode material. Indeed, Li could be inserted below 1.5 V, albeit with relatively low capacity (Figure 7). On the first discharge, a capacity of nearly 90 mAh/g is reached, compared to a theoretical capacity of 173 mAh/g for a one-electron reaction.

$\text{LiCo}_{0.5}\text{Ti}_{1.5}\text{O}_4$ and $\text{LiCo}_{0.5}\text{Sn}_{1.5}\text{O}_4$

Although $\text{LiCo}_{0.5}\text{Ti}_{1.5}\text{O}_4$ and $\text{LiCo}_{0.5}\text{Sn}_{1.5}\text{O}_4$ contain Co^{2+} , suggesting their use as high voltage cathode materials, the reversible capacity is very low. For $\text{LiCo}_{0.5}\text{Ti}_{1.5}\text{O}_4$, a capacity of ~65 mAh/g is observed on charging to 4.8 V, but much of this is likely associated with electrolyte oxidation as only ~16 mAh/g is observed on the subsequent discharge (Figure 8a). By the fourth cycle, the discharge capacity is less than 5 mAh/g. For $\text{LiCo}_{0.5}\text{Sn}_{1.5}\text{O}_4$, an initial charge capacity of ~47 mAh/g is observed on charging to 4.8 V, but only ~6 mAh/g is observed on the following discharge (Figure 8b). The lower cutoff voltage in both cases was 2.5 V to avoid conversion reactions associated with reduction to Co or Sn metal. It is possible that the poor electrochemical performance of both compounds results from the poor electronic conductivity; the active ion, Co^{2+} is somewhat dilute in a framework of $d^0 \text{Ti}^{4+}$ cations, which results in a highly insulating material. The somewhat contrasting behavior of $\text{LiFe}_{0.5}\text{Ti}_{1.5}\text{O}_4$ could be explained by the fact that the $\text{Fe}^{3+/2+}$ and $\text{Ti}^{4+/3+}$ redox couples are much closer in voltage than those of $\text{Co}^{4+/2+}$ and $\text{Ti}^{4+/3+}$. As a result, charge transfer reactions are more favorable in $\text{LiFe}_{0.5}\text{Ti}_{1.5}\text{O}_4$, likely resulting in higher hopping conductivity.

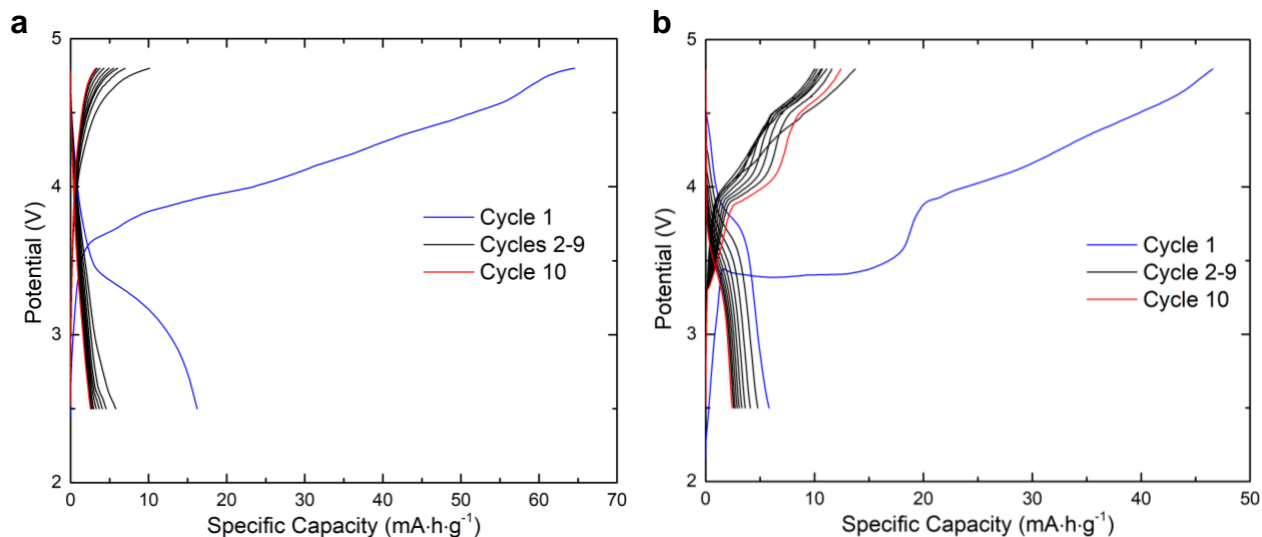


Figure 8 Galvanostatic cycling curves for (a) $\text{LiCo}_{0.5}\text{Ti}_{1.5}\text{O}_4$ and (b) $\text{LiCo}_{0.5}\text{Sn}_{1.5}\text{O}_4$ cycled at $C/20$.

Li_{0.96}Rh_{0.96}Ti_{1.04}O₄

Approximately 1/3 of the theoretical capacity is observed for $\text{Li}_{0.96}\text{Rh}_{0.96}\text{Ti}_{1.04}\text{O}_4$ (~40 mAh/g), accompanied by high polarization. (Figure 9) Reportedly, the $\text{Rh}^{4+/3+}$ redox couple can be accessed in LiRhO_2 , $\text{Li}_{1.2}\text{Rh}_{0.8}\text{O}_2$, and LiRh_2O_4 , though the reaction is known to be incomplete in the voltage range explored in this work.⁶¹⁻⁶³ Recent work from Chamorro et al. has shown that LiRh_2O_4 can only be electrochemically delithiated to about $\text{Li}_{0.55}\text{Rh}_2\text{O}_4$ and the oxidized rhodate is apparently unstable with lithium electrolytes.⁶⁴ However, spinel structured LiRh_2O_4 can be fully chemically delithiated, which presents an interesting future direction for exploration of the post-spinel LiRhTiO_4 .⁶⁴

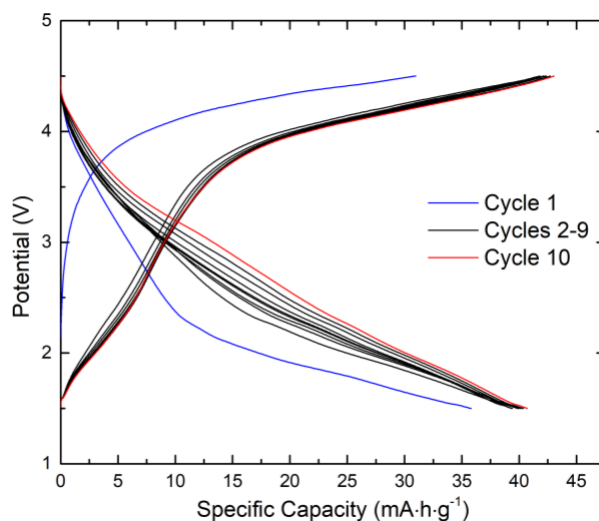


Figure 9 Galvanostatic cycling curves for post-spinel LiRhTiO_4 cycled at $C/20$.

Operando X-ray diffraction. $\text{Li}_{0.96}\text{Mn}_{0.96}\text{Sn}_{0.74}\text{Ti}_{0.30}\text{O}_4$, which cycles between $\sim\text{Li}_{0.3}\text{Mn}_{0.96}\text{Sn}_{0.74}\text{Ti}_{0.30}\text{O}_4$ and $\sim\text{Li}_{1.4}\text{Mn}_{0.96}\text{Sn}_{0.74}\text{Ti}_{0.30}\text{O}_4$, was selected for *operando* X-ray diffraction measurements to track the evolution of the post-spinel lattice during lithium extraction and tunnel stuffing (insertion beyond one Li per f.u.) (Figures 10 and 11). A sequential Rietveld refinement was performed on 233 integrated diffraction images collected over 13 h corresponding to the first charge, followed by two full cycles. Lattice parameter evolution with estimated standard deviations, and changes in metal positions, are shown in Supplementary Information Figures S3–S4. On the initial delithiation to 4.5 V, the a and c axes contracted 2.9% and 0.9%, respectively,

while the b dimension along the tunnels was remarkably unchanged (final = -0.004% , max. deviation = 0.026%). On 1st discharge, the a and c axes expanded toward their initial dimensions but the crystallographic changes were not a mirror reversal. As lithium was inserted down to 1.5 V, the b axis did become active. The volume change over a full discharge corresponding to the insertion of 1.1 lithium per f.u. was 6.8% . The majority of this expansion can be attributed to the a axis. Subsequent charge/discharge cycles followed the same trends. While the electrochemical behavior of the free-standing electrode in this XRD experiment is similar to that of the conventionally cast films, the former is a thicker and mechanically weaker electrode that exhibited a lower reversible capacity.

The diffraction patterns of the first two cycles are shown in Figure 11. There appears to be a subtle two-phase reaction in both the charge and discharge data, indicating that the calcium ferrite structure does not expand continuously. The symmetry does not change through this subtle transition so it suggests a miscibility gap rather than a structural rearrangement. The two-phase reaction corresponds to the inflection point in the voltage curves at about 20 mins into both the first charge and first discharge.

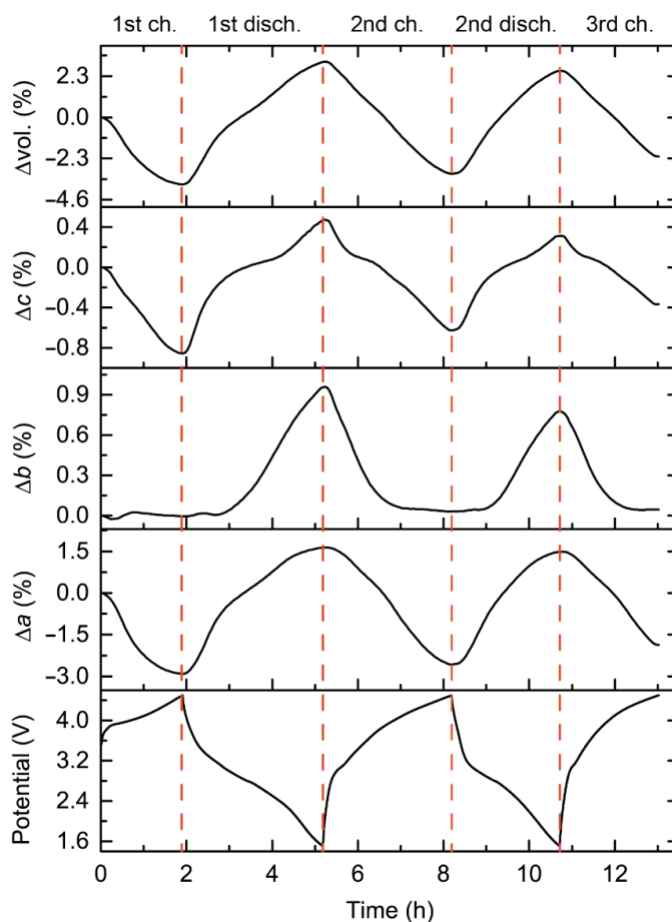


Figure 10 Structural evolution of $\text{Li}_{0.96}\text{Mn}_{0.96}\text{Sn}_{0.74}\text{Ti}_{0.30}\text{O}_4$ on the first charge and the subsequent two full cycles between 4.5 and 1.5 V vs. Li^+/Li at a rate of $C/3$. Lattice parameter changes are derived from sequential Rietveld refinement of 233 synchrotron diffraction patterns collected over 13 hours.

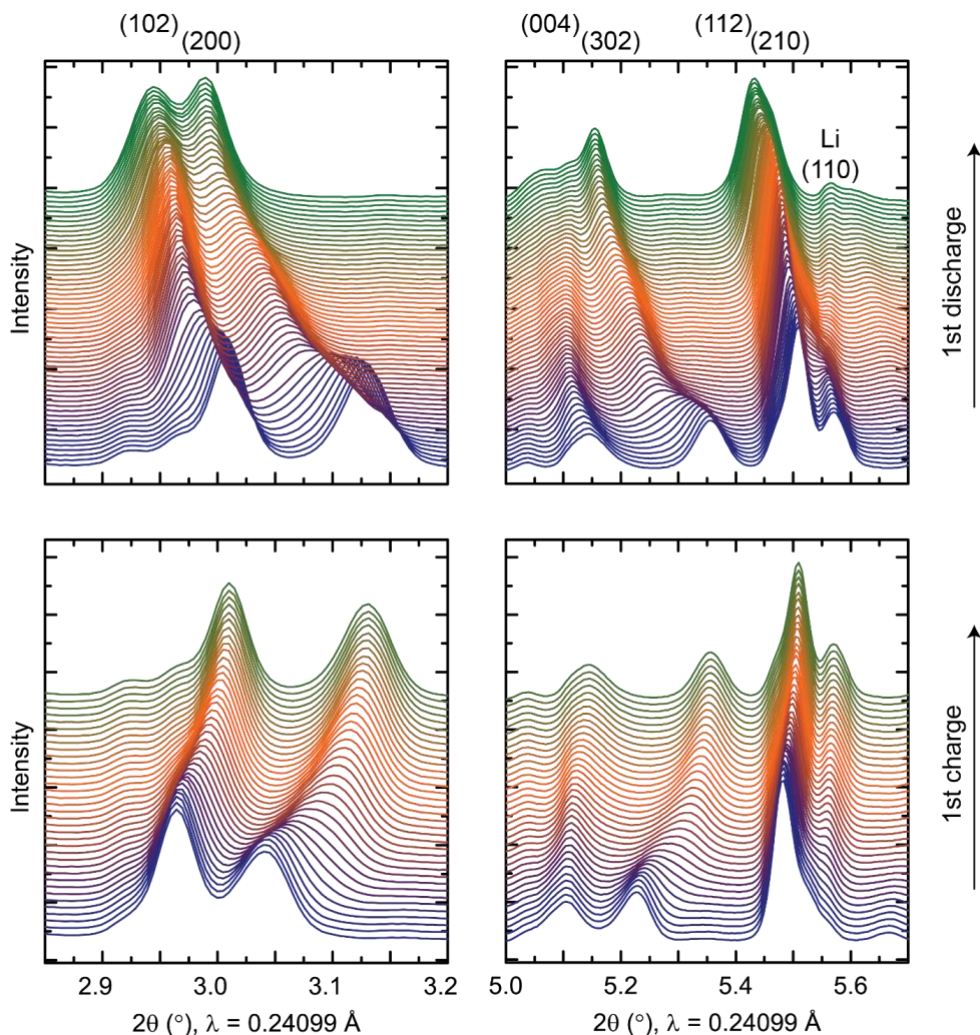


Figure 11 Synchrotron X-ray diffraction patterns of $\text{Li}_{0.96}\text{Mn}_{0.96}\text{Sn}_{0.74}\text{Ti}_{0.30}\text{O}_4$ on the first charge and first discharge between 4.5 and 1.5 V vs. Li^+/Li at a rate of $C/3$. Selected calcium ferrite reflections and the (110) reflection from the lithium metal anode are denoted.

Energy landscape of stoichiometric and Li-stuffed post-spinels. In prior studies on post-spinel compounds, the focus has primarily been on the electrochemistry of $\text{Li}/\text{Na}/\text{Mg}$ with up to one alkali or alkaline-earth ion per $AM_xM^{2-x}O_4$ formula unit.^{29, 32} However, our investigation revealed that in some frameworks such as VTiO_4 , MnSnO_4 , and FeTiO_4 , Li ions can be inserted up to a maximum of two per formula unit, as reported in the synthesis of $\text{Li}_2\text{FeTiO}_4$.³³ While the positions of Li in the FeTiO_4 framework have been reported based on XRD experiments, we sought to clarify this by computationally evaluating the energy landscape within the tunnels of the calcium ferrite framework.

Figure 12 presents the energy for Li at different positions in the tunnel of $\text{Li}_x\text{MnSnO}_4$. Lithium positions were varied in the bc plane to generate candidate Li sites (Figure 12a). The position along the a axis was set to match that of Ca in CaFe_2O_4 post-spinels. The energy landscape in Figure 12a suggests that, in the absence of cation stuffing, the lithium ion in Li-post-spinels occupies the same position as calcium in CaFe_2O_4 post-spinels. Detailed structural data can be found in Table S1.

To compute the energy landscape of Li-stuffed $\text{Li}_{1+x}\text{MnSnO}_4$, additional Li ions were added to the pristine LiMnSnO_4 structure. After relaxation of DFT forces, the original Li ion within each tunnel relocated to the edge of said tunnel, as shown in Figure 12b. To determine the position of the new ‘stuffed’ Li ion within the tunnel, a bc plane energy landscape was calculated (assuming the new lithium to be intermediate between existing lithium ions in the a axis) (Figure 12b). Two energy minima are identified in the energy landscape. Although both sites have comparable energy, we selected the position with slightly lower energy ($b = 0.29$, $c = 0.83$) for further calculations. Detailed positions of the stuffed Li ions can be found in Table S1.

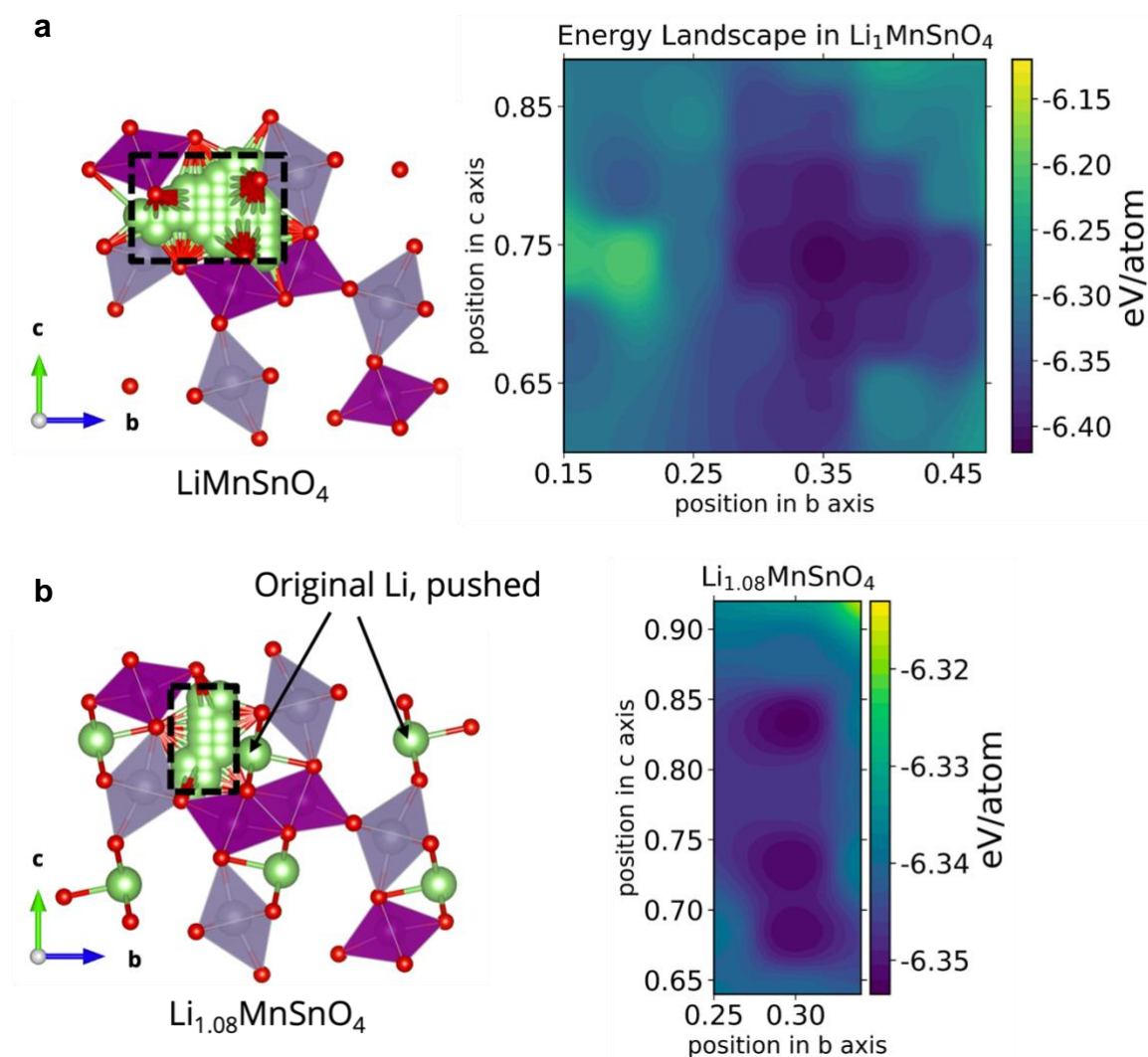


Figure 12 DFT-calculated energy landscape for different lithium positions in (a) stoichiometric LiMnSnO_4 and (b) lithium-stuffed $\text{Li}_{1.08}\text{MnSnO}_4$. The bright green atoms in the structure figures represent the calculated Li ion positions. The energy landscapes show interpolated DFT energies for the various lithium positions.

Lithium post-spinel partial density of states. Electrochemical lithium extraction and insertion of the Li post-spinel compounds has revealed a relatively low voltage (~ 1.5 V) feature when $M' =$

Ti in the $\text{Li}_x\text{M}'\text{M}'_{2-x}\text{O}_4$ formula unit, a characteristic not observed in the $M' = \text{Sn}$ analogues. This is consistent with $\text{Ti}^{4+/3+}$ redox in, *e.g.*, $\text{Li}_4\text{Ti}_5\text{O}_{12}$ and polymorphs of TiO_2 . To gain insights on the role of the M' metal in lithium post-spinel compounds, partial density of states (DOS) plots were computed for $\text{Li}_x\text{MnSnO}_4$ and Li_xVTiO_4 . Figure 13a shows the variation of the partial Mn/Sn DOS at different Li levels. Unoccupied electronic states from tin are generally more than 2 eV into the conduction band and remain unchanged upon lithium insertion. On the other hand, manganese states are filled during lithiation and shift from the conduction into the valence band, indicating that Mn is the only redox-active metal in the $\text{Li}_x\text{MnSnO}_4$ compound from $0 \leq x \leq 2$.

In contrast, Li_xVTiO_4 exhibits overlapping vanadium and titanium electronic states, as depicted in Figure 13b. Vanadium states dominate the conduction band at low Li concentrations ($x < 1.0$) and appears to be reduced first. At the composition LiVTiO_4 , titanium states begin to dominate the conduction band, indicating that the $\text{Ti}^{4+/3+}$ couple becomes electrochemically active upon deeper lithium insertion. Overall, the electrochemical features of the post-spinels in this work can be summarized as a higher voltage process for the mid-to-late transition metal $M^{4+/3+}$ redox couple followed by a 1.5 V $\text{Ti}^{4+/3+}$ redox couple when $M' = \text{Ti}$. Vanadium reduction below V(III) is also indicated.

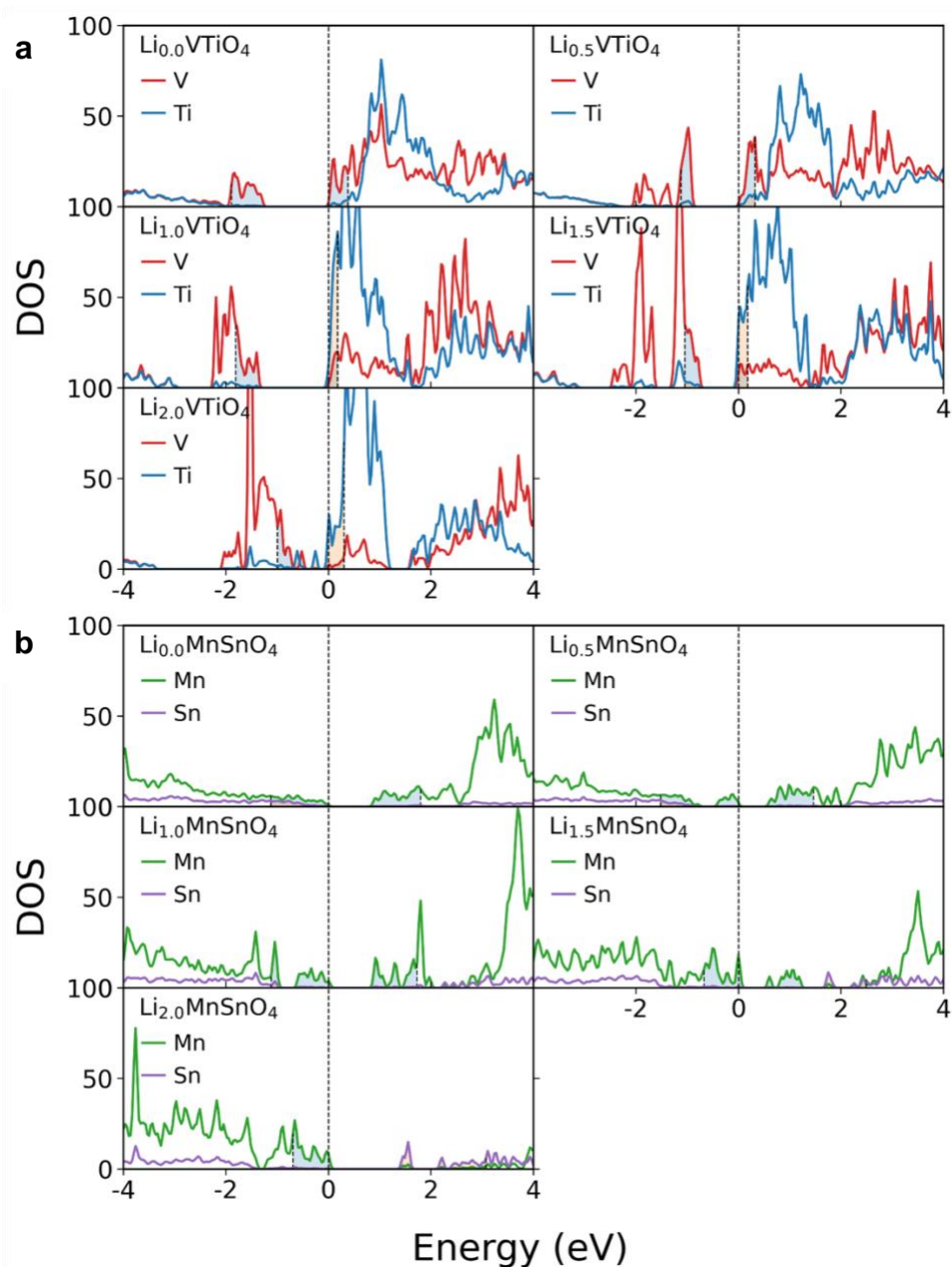


Figure 13 Computed DOS for (a) $\text{Li}_x\text{MnSnO}_4$ and (b) Li_xVTiO_4 for different Li concentrations ($x = 0, 0.5, 1.0, 1.5, 2.0$). The dashed line at the center denotes the Fermi level. The shaded regions on either side of the Fermi level are the valence and conduction band DOS corresponding to 0.5 frontier electrons per $\text{Li}_x\text{MM}'\text{O}_4$ formula unit.

Thermodynamic stability of Li post-spinels as a function of (de)lithiation. Convex hull calculations were carried out to understand the stability of phases in the Li-CF chemical space. The energy above the convex hull of stability is calculated for various combinations of octahedral transition metals and at varying degrees of lithiation including dilute and stuffed. Lithium positions according to the preceding section were used and, when partially occupied, orderings were

attempted with the three lowest electrostatic energy configurations. Computed energies above the convex hull (E_{hull}) of Li-CF phases at 0 K are shown in Figure 14; no entropic terms are included. All phases are above the hull except $\text{LiFe}_{0.5}\text{Sn}_{1.5}\text{O}_4$.

As expected, $\text{LiMM}'\text{O}_4$ compounds have lower E_{hull} values than their over- or under-stoichiometric modifications. Ti^{4+} and Sn^{4+} lithium post-spinels are more stable than those with Zr^{4+} , suggesting that the Zr^{4+} analogues may be more difficult to synthesize and may decompose more easily during Li cycling. Considering the successful ion exchange and electrochemical insertion/extraction of $\text{Li}_{0.96}\text{V}_{0.96}\text{Ti}_{1.04}\text{O}_4$, $\text{LiFe}_{0.5}\text{Ti}_{1.5}\text{O}_4$, $\text{Li}_{0.96}\text{Cr}_{0.96}\text{Ti}_{1.04}\text{O}_4$ and LiMnSnO_4 , E_{hull} up to 50 meV/atom for the $\text{LiMM}'\text{O}_4$ stoichiometry appears to be accessible and may be a useful cutoff for filtering promising Li post-spinel compounds.

Upon Li extraction, the compounds generally become increasingly unstable, suggesting that it may be difficult to extract all of the lithium without inducing decomposition reactions. Importantly, while pristine LiMSnO_4 post-spinel compounds are more stable than their Ti^{4+} analogues, the Ti^{4+} compounds (except $M = \text{Rh}^{3+}$) have lower E_{hull} upon delithiation and thus may be preferred for electrode applications.

$\text{LiMM}'\text{O}_4$ post-spinels are also destabilized by lithium insertion. Considering the high E_{hull} values here (larger than 100 meV/atom), it is likely that kinetic stability will be important to promising compounds. Considering that Li_xVTiO_4 and $\text{Li}_x\text{MnSnO}_4$ can experimentally accommodate up to 1.5 Li, about ~ 120 meV/atom could be suggested as secondary screening standards for Li insertion.

Thermodynamic calculations reveal that Li_xVTiO_4 and $\text{Li}_x\text{MnSnO}_4$ exhibit the highest degree of stability throughout the process of Li extraction and insertion. This observation aligns with the experimental electrochemical outcomes. As elucidated in the preceding section, the electrochemical performance of Li_xVTiO_4 can be attributed to mixed vanadium/titanium redox centers, while the multielectron redox adaptability of manganese underpins $\text{Li}_x\text{MnSnO}_4$. Although $\text{Li}_x\text{Fe}_{0.5}\text{Sn}_{1.5}\text{O}_4$ is untested and $\text{Li}_x\text{Co}_{0.5}\text{Sn}_{1.5}\text{O}_4$ did not show promising electrochemistry in this initial study, their E_{hull} values are encouraging.

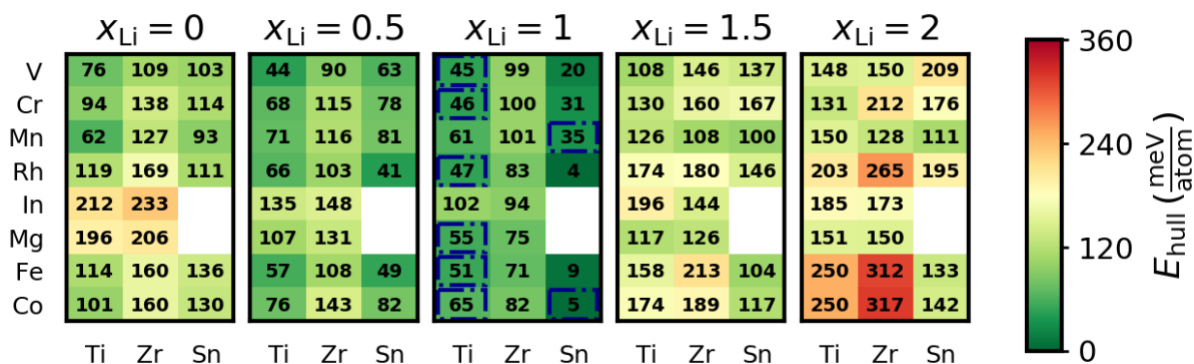


Figure 14 Computed energy above hull of $\text{Li}_x\text{M}^{3+}\text{M}'^{4+}\text{O}_4$ and $\text{LiM}^{2+}_{0.5}\text{M}'^{4+}_{1.5}\text{O}_4$ CF phases with lithium contents $x = 0, 0.5, 1.0, 1.5,$ and 2.0 . Experimentally examined compounds are indicated by blue outlined boxes in $x_{\text{Li}} = 1$.

Lithium hopping barriers in the post-spinel structure. To understand Li^+ transport as a function of lithium concentration, one lithium (per supercell) was removed from dilute $\text{Li}_{0.5}\text{MM}'\text{O}_4$, stoichiometric $\text{Li}_{1.0}\text{MM}'\text{O}_4$, and stuffed $\text{Li}_{1.5}\text{MM}'\text{O}_4$ structures to form $\text{Li}_{0.42}\text{MM}'\text{O}_4$, $\text{Li}_{0.92}\text{MM}'\text{O}_4$, and $\text{Li}_{1.42}\text{MM}'\text{O}_4$ ($M = \text{Mn}, \text{V}$; $M' = \text{Sn}, \text{Ti}$). The computed barrier for $\text{Li}_{0.92}\text{MnSnO}_4$ is similar to that found in a previous study,²⁹ which highlighted that the Li hopping barriers in Mn-based post-spinels are low, smaller than 0.2 eV. Notably, our results show that both dilute and stuffed post-spinel structures exhibit an increased barrier, reaching 0.6 eV, as illustrated in Figure 15a. This increased barrier may account for the inability to achieve Li stuffing up to $\text{Li}_2\text{MnSnO}_4$ despite the similar energy above the hull of $\text{Li}_{1.5}\text{MnSnO}_4$ and $\text{Li}_2\text{MnSnO}_4$. In contrast, Li_xVTiO_4 shows relatively consistent migration barriers of 0.23, 0.31, and 0.37 eV for dilute, near-stoichiometric, and stuffed configurations, respectively (Figure 15b).

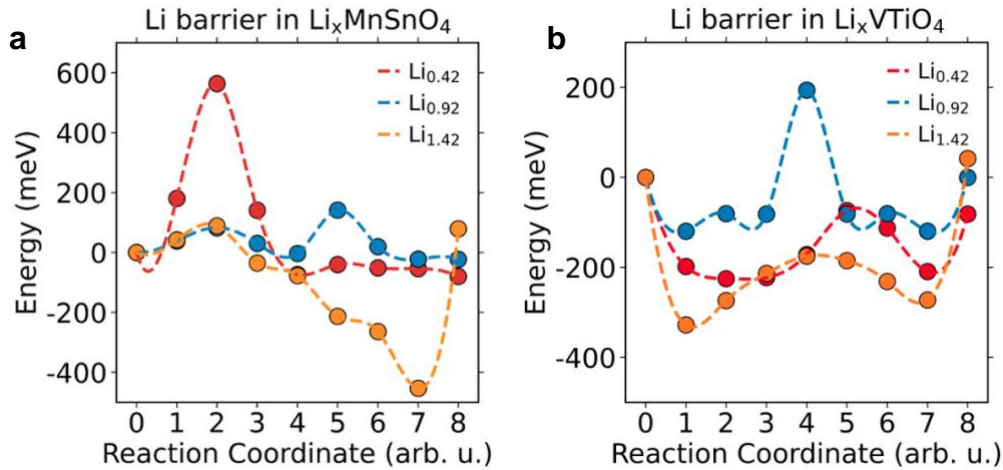


Figure 15 Computed energy barriers for lithium transport in $\text{Li}_{0.42}\text{MM}'\text{O}_4$, near-stoichiometric $\text{Li}_{0.92}\text{MM}'\text{O}_4$, and stuffed $\text{Li}_{1.42}\text{MM}'\text{O}_4$ phases. (a) $M = \text{Mn}$, $M' = \text{Sn}$. (b) $M = \text{V}$, $M' = \text{Ti}$.

Electrochemical rate and durability testing. The rate and cycling capabilities of $\text{Li}_{0.96}\text{V}_{0.96}\text{Ti}_{1.04}\text{O}_4$ (LVT-Ar) were examined. $\text{Li}_{0.96}\text{V}_{0.96}\text{Ti}_{1.04}\text{O}_4$ could be cycled at relatively high rates; the capacities at 1C and 2C are $\sim 80\%$ and $\sim 70\%$ of the C/10 capacity, respectively (Figure 16a). This is consistent with the low barriers calculated for lithium mobility in the previous section. The capacity retention is also high (Figure 16b). When cycled at a rate of C/2.5 between 4.2 V and 1.0 V, the first cycle capacity retention is 96% and the cumulative capacity loss from the 2nd to the 100th cycle is only 1%. When combined with the *operando* and *ex situ* PXRD of cycled $\text{Li}_{0.96}\text{Mn}_{0.96}\text{Sn}_{0.74}\text{Ti}_{0.30}\text{O}_4$ and $\text{Li}_{0.96}\text{Cr}_{0.96}\text{Ti}_{1.04}\text{O}_4$, the data suggest that the CF structure is a kinetically stable insertion host in lithium-ion battery cells at room temperature, even though the

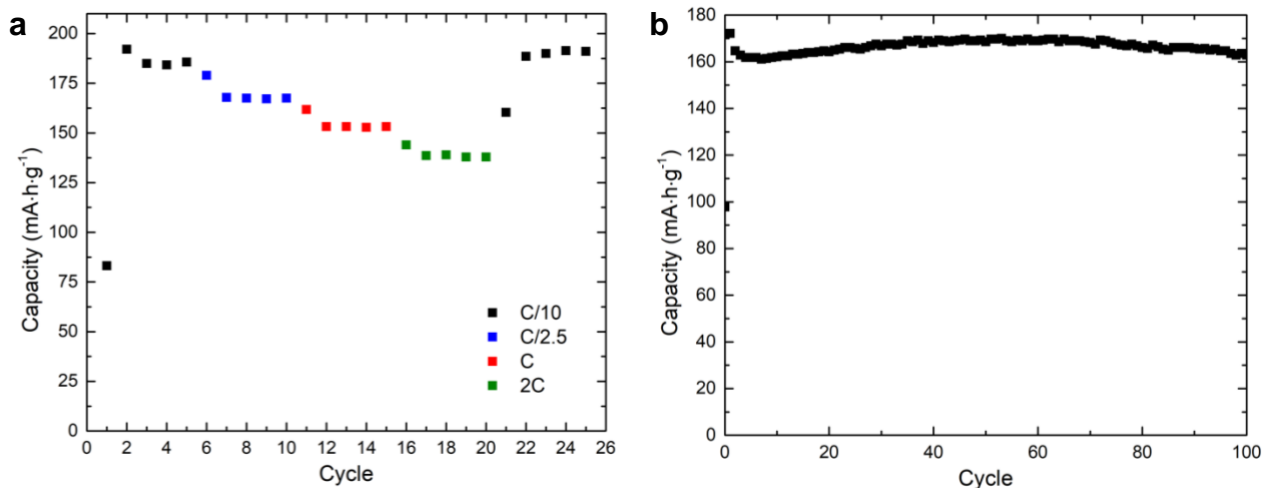


Figure 16 (a) Charge capacity during rate testing of $\text{Li}_{0.96}\text{V}_{0.96}\text{Ti}_{1.04}\text{O}_4$ and (b) capacity of $\text{Li}_{0.96}\text{V}_{0.96}\text{Ti}_{1.04}\text{O}_4$ cycled between 4.2 V and 1.0 V at C/2.5 for 100 cycles.

CF structure is not expected to be thermodynamically stable at any degree of lithiation.

In this broad comparative synthetic and electrochemical study of post-spinel CF compounds, it was observed that the capacity, average voltage, rate, and stability of $\text{Li}_{0.96}\text{V}_{0.96}\text{Ti}_{1.04}\text{O}_4$ are on par with vanadium-based disordered rocksalt structures.⁶⁵⁻⁶⁶ This is particularly interesting because the CF phase is neither nanostructured nor carbon-coated and reaches this capacity with an upper cutoff voltage of 4.2 V that is within the stability window of standard battery electrolytes while disordered rocksalt phases access their high capacities at voltages up to 4.6–4.8 V and are typically nanostructured and carbon-coated to overcome poor native electronic conductivity.

Conclusions

Lithium post-spinels have been synthesized at ambient pressure via ion-exchange reactions and their electrochemical lithium extraction and insertion have been studied as electrodes in lithium batteries. Lithium can be reversibly extracted at high voltages from LiMnSnO_4 , $\text{Li}_{0.96}\text{Mn}_{0.96}\text{Sn}_{1.04-x}\text{Ti}_x\text{O}_4$, $\text{Li}_{0.96}\text{V}_{0.96}\text{Ti}_{1.04}\text{O}_4$, $\text{Li}_{0.96}\text{Cr}_{0.96}\text{Ti}_{1.04}\text{O}_4$, and $\text{LiFe}_{0.5}\text{Ti}_{1.5}\text{O}_4$, but only about half of the available lithium is extracted in each case. Each of these compounds, in addition to $\text{LiMg}_{0.5}\text{Ti}_{1.5}\text{O}_4$ can also accommodate more than one Li^+ per formula unit. Lithium insertion is observed at low voltages, with the $\text{Mn}^{3+/2+}$ redox couple accessed for the manganese compounds, and the $\text{Ti}^{4+/3+}$ couple accessed for the titanates. In most cases, only about 0.5 additional lithium atoms are inserted

per formula unit. However, the fact that an alternative synthesis method for $\text{Li}_{0.96}\text{V}_{0.96}\text{Ti}_{1.04}\text{O}_4$ enabled lithium-stuffed $\sim\text{Li}_2\text{VTiO}_4$ and that CF- LiFeTiO_4 has previously been reported to reach $\text{Li}_2\text{FeTiO}_4$ suggests the possibility that additional capacity could be accessed for the compounds reported in this work via tailored synthetic methods (e.g., sol-gel synthesis) and materials/electrode engineering. There is evidence for multielectron Mn redox in manganese post spinels. Electrochemical and diffraction data suggest that the calcium ferrite structure is kinetically stable and a promising host structure for Li-ion batteries. Stability and electronic structure calculations aid redox mechanistic assignments and suggest promising screening criteria for future metastable lithium post-spinel electrodes.

Supporting Information

Lithium post-spinel SEM images, additional ^7Li solid-state NMR spectra, absolute lattice parameters and metal fractional coordinates as a function of lithium content in $\text{Li}_{0.96}\text{Mn}_{0.96}\text{Sn}_{0.74}\text{Ti}_{0.30}\text{O}_4$ from *operando* synchrotron XRD, fractional coordinates of DFT-relaxed LiMnSnO_4 and $\text{Li}_{1.08}\text{MnSnO}_4$ as computed by GGA+U.

Acknowledgements

This work was supported by the Joint Center for Energy Storage Research (JCESR), an Energy Innovation Hub funded by the U.S. Department of Energy, Office of Science, Office of Basic Energy Sciences. Use of the Advanced Photon Source at Argonne National Laboratory was supported by the U. S. Department of Energy, Office of Science, Office of Basic Energy Sciences, under Contract No. DE-AC02-06CH11357. This work made use of the Jerome B. Cohen X-Ray Diffraction Facility supported by the MRSEC program of the National Science Foundation (DMR-1720139) at the Materials Research Center of Northwestern University and the Soft and Hybrid Nanotechnology Experimental (SHyNE) Resource (NSF ECCS-2025633). This work made use of the IMSERC NMR facilities at Northwestern University, which have received support from the Soft and Hybrid Nanotechnology Experimental (SHyNE) Resource (NSF ECCS-2025633), International Institute of Nanotechnology, and Northwestern University. This research used resources of the National Energy Research Scientific Computing Center (NERSC), a U.S. Department of Energy Office of Science User Facility located at Lawrence Berkeley National Laboratory, operated under Contract No. DE-AC02-05CH11231. Computational resources were also provided by the Extreme Science and Engineering Discovery Environment (XSEDE) resource Stampede2 through allocation TG-DMR970008S, which is supported by the National Science Foundation grant number ACI1053575.

References

1. Huang, Y.; Dong, Y.; Li, S.; Lee, J.; Wang, C.; Zhu, Z.; Xue, W.; Li, Y.; Li, J., Lithium Manganese Spinel Cathodes for Lithium-Ion Batteries. *Advanced Energy Materials* **2021**, *11* (2), 2000997.
2. Ferg, E.; Gummow, R. J.; de Kock, A.; Thackeray, M. M., Spinel Anodes for Lithium-Ion Batteries. *Journal of The Electrochemical Society* **1994**, *141* (11), L147.
3. Thackeray, M. M.; Amine, K., $\text{Li}_4\text{Ti}_5\text{O}_{12}$ spinel anodes. *Nature Energy* **2021**, *6* (6), 683-683.
4. Thackeray, M.; De Kock, A.; Rossouw, M.; Liles, D.; Bittihn, R.; Hoge, D., Spinel electrodes from the Li-Mn-O system for rechargeable lithium battery applications. *Journal of the Electrochemical Society* **1992**, *139* (2), 363.
5. Zhang, X.; Yang, M.; Zhao, X.; Wang, Y.; Wang, M.; Ma, L., The spinel phase LiMnTiO_4 as a potential cathode for rechargeable lithium ion batteries. *Journal of Materials Science: Materials in Electronics* **2015**, *26* (9), 6366-6372.
6. Thackeray, M. M.; Johnson, P. J.; de Picciotto, L. A.; Bruce, P. G.; Goodenough, J. B., Electrochemical extraction of lithium from LiMn_2O_4 . *Materials Research Bulletin* **1984**, *19* (2), 179-187.
7. Sigala, C.; Guyomard, D.; Verbaere, A.; Piffard, Y.; Tournoux, M., Positive electrode materials with high operating voltage for lithium batteries: $\text{LiCr}_y\text{Mn}_{2-y}\text{O}_4$ ($0 \leq y \leq 1$). *Solid State Ionics* **1995**, *81* (3), 167-170.
8. Kim, J. H.; Myung, S. T.; Yoon, C. S.; Kang, S. G.; Sun, Y. K., Comparative Study of $\text{LiNi}_{0.5}\text{Mn}_{1.5}\text{O}_{4-\delta}$ and $\text{LiNi}_{0.5}\text{Mn}_{1.5}\text{O}_4$ Cathodes Having Two Crystallographic Structures: $Fd\bar{3}m$ and $P4332$. *Chemistry of Materials* **2004**, *16* (5), 906-914.
9. Amin, R.; Muralidharan, N.; Petla, R. K.; Yahia, H. B.; Al-Hail, S. A. J.; Essehli, R.; Daniel, C.; Khaleel, M. A.; Belharouak, I., Research advances on cobalt-free cathodes for Li-ion batteries-The high voltage $\text{LiMn}_{1.5}\text{Ni}_{0.5}\text{O}_4$ as an example. *Journal of Power Sources* **2020**, *467*, 228318.
10. Ohzuku, T.; Ueda, A.; Yamamoto, N., Zero-Strain Insertion Material of $\text{Li}[\text{Li}_{1/3}\text{Ti}_{5/3}]\text{O}_4$ for Rechargeable Lithium Cells. *Journal of The Electrochemical Society* **1995**, *142* (5), 1431.
11. Colbow, K.; Dahn, J.; Haering, R., Structure and electrochemistry of the spinel oxides LiTi_2O_4 and $\text{Li}_{4/3}\text{Ti}_{5/3}\text{O}_4$. *Journal of Power Sources* **1989**, *26* (3-4), 397-402.
12. Chen, C.; Vaughney, J.; Jansen, A. N.; Dees, D.; Kahaian, A.; Goacher, T.; Thackeray, M., Studies of Mg-substituted $\text{Li}_{4-x}\text{Mg}_x\text{Ti}_5\text{O}_{12}$ spinel electrodes ($0 \leq x \leq 1$) for lithium batteries. *Journal of the Electrochemical Society* **2001**, *148* (1), A102.

13. Ohzuku, T.; Tatsumi, K.; Matoba, N.; Sawai, K., Electrochemistry and Structural Chemistry of $\text{Li}[\text{CrTi}]\text{O}_4$ ($Fd\bar{3}m$) in Nonaqueous Lithium Cells. *Journal of The Electrochemical Society* **2000**, *147* (10), 3592.
14. Aravindan, V.; Ling, W. C.; Madhavi, S., LiCrTiO_4 : A High-Performance Insertion Anode for Lithium-Ion Batteries. *ChemPhysChem* **2012**, *13* (14), 3263-3266.
15. Barker, J.; Saidi, M. Y.; Swoyer, J. L., Electrochemical insertion properties of lithium vanadium titanate, LiVTiO_4 . *Solid State Ionics* **2004**, *167* (3), 413-418.
16. De Picciotto, L.; Thackeray, M., Insertion/extraction reactions of lithium with LiV_2O_4 . *Materials research bulletin* **1985**, *20* (12), 1409-1420.
17. Chen, R.; Knapp, M.; Yavuz, M.; Heinzmann, R.; Wang, D.; Ren, S.; Trouillet, V.; Lebedkin, S.; Doyle, S.; Hahn, H.; Ehrenberg, H.; Indris, S., Reversible Li^+ Storage in a LiMnTiO_4 Spinel and Its Structural Transition Mechanisms. *The Journal of Physical Chemistry C* **2014**, *118* (24), 12608-12616.
18. Robertson, A.; Tukamoto, H.; Irvine, J., $\text{Li}_{1+x}\text{Fe}_{1-3x}\text{Ti}_{1+2x}\text{O}_4$ ($0.0 \leq x \leq 0.33$) Based Spinel: Possible Negative Electrode Materials for Future Li-Ion Batteries. *Journal of the Electrochemical Society* **1999**, *146* (11), 3958.
19. Fey, G. T. K.; Li, W.; Dahn, J. R., LiNiVO_4 : A 4.8 Volt Electrode Material for Lithium Cells. *Journal of The Electrochemical Society* **1994**, *141* (9), 2279.
20. Sai Gautam, G.; Canepa, P.; Urban, A.; Bo, S.-H.; Ceder, G., Influence of inversion on Mg mobility and electrochemistry in spinels. *Chemistry of Materials* **2017**, *29* (18), 7918-7930.
21. Ringwood, A. E., Phase transformations and the constitution of the mantle. *Physics of the Earth and Planetary Interiors* **1970**, *3*, 109-155.
22. Akaogi, M., Phase transitions of minerals in the transition zone and upper part of the lower mantle. In *Advances in High-Pressure Mineralogy*, Ohtani, E., Ed. Geological Society of America: 2007; Vol. 421, p 0.
23. Iskrina, A. V.; Bobrov, A. V.; Spivak, A. V., Post-Spinel Phases in the Earth's Mantle. *Geochemistry International* **2022**, *60* (4), 311-324.
24. Iskrina, A. V.; Bobrov, A. V.; Spivak, A. V.; Kuzmin, A. V.; Chariton, S.; Fedotenko, T.; Dubrovinsky, L. S., The new $\text{Ca}(\text{Fe},\text{Al})_2\text{O}_4$ phase with calcium ferrite-type structure, a likely carrier of Al in the transition zone and lower mantle. *Journal of Physics and Chemistry of Solids* **2022**, *171*, 111031.
25. Uenver-Thiele, L.; Woodland, A. B.; Boffa Ballaran, T.; Miyajima, N.; Frost, D. J., Phase relations of Fe-Mg spinels including new high-pressure post-spinel phases and implications for natural samples. **2017**, *102* (10), 2054-2064.
26. Decker, B. F.; Kasper, J. S., The structure of calcium ferrite. *Acta Crystallographica* **1957**, *10* (4), 332-337.
27. Giesber, H. G.; Pennington, W. T.; Kolis, J. W., Redetermination of CaMn_2O_4 . *Acta Crystallographica Section C* **2001**, *57* (4), 329-330.
28. Rogge, M. P.; Caldwell, J. H.; Ingram, D. R.; Green, C. E.; Geselbracht, M. J.; Siegrist, T., A New Synthetic Route to Pseudo-Brookite-Type CaTi_2O_4 . *Journal of Solid State Chemistry* **1998**, *141* (2), 338-342.
29. Ling, C.; Mizuno, F., Phase stability of post-spinel compound AMn_2O_4 ($A = \text{Li}, \text{Na}, \text{or Mg}$) and its application as a rechargeable battery cathode. *Chemistry of Materials* **2013**, *25* (15), 3062-3071.
30. Zhu, Y.-F.; Xiao, Y.; Dou, S.-X.; Kang, Y.-M.; Chou, S.-L., Spinel/Post-spinel engineering on layered oxide cathodes for sodium-ion batteries. *eScience* **2021**, *1* (1), 13-27.
31. Mamiya, M.; Tokiwa, K.; Akimoto, J., Soft chemical synthesis and electrochemical properties of calcium ferrite-type $\text{Li}_x\text{Mn}_2\text{O}_4$. *Journal of Power Sources* **2016**, *310*, 12-17.
32. Nolis, G.; Gallardo-Amores, J. M.; Serrano-Sevillano, J.; Jahrman, E.; Yoo, H. D.; Hu, L.; Hancock, J. C.; Bolotnikov, J.; Kim, S.; Freeland, J. W.; Liu, Y.-S.; Poepelmeier, K. R.; Seidler, G. T.; Guo, J.; Alario-Franco, M. A.; Casas-Cabanas, M.; Morán, E.; Cabana, J., Factors Defining the Intercalation Electrochemistry of CaFe_2O_4 -Type Manganese Oxides. *Chemistry of Materials* **2020**, *32* (19), 8203-8215.

33. Bruno, S. R.; Blakely, C. K.; Clapham, J. B.; Davis, J. D.; Bi, W.; Alp, E. E.; Poltavets, V. V., Synthesis and electrochemical properties of novel LiFeTiO_4 and $\text{Li}_2\text{FeTiO}_4$ polymorphs with the CaFe_2O_4 -type structures. *Journal of Power Sources* **2015**, 273, 396-403.
34. Jung, Y. H.; Kim, D. K.; Hong, S.-T., Synthesis, structure, and electrochemical Li-ion intercalation of LiRu_2O_4 with CaFe_2O_4 -type structure. *Journal of power sources* **2013**, 233, 285-289.
35. Mukai, K.; Uyama, T.; Yamada, I., Structural and Electrochemical Analyses on the Transformation of CaFe_2O_4 -Type LiMn_2O_4 from Spinel-Type LiMn_2O_4 . *ACS omega* **2019**, 4 (4), 6459-6467.
36. Sun, X.; Blanc, L.; Nolis, G. M.; Bonnicksen, P.; Cabana, J.; Nazar, L. F., $\text{NaV}_{1.25}\text{Ti}_{0.75}\text{O}_4$: A Potential Post-Spinel Cathode Material for Mg Batteries. *Chemistry of Materials* **2018**, 30 (1), 121-128.
37. Hannah, D. C.; Gautam, G. S.; Canepa, P.; Rong, Z.; Ceder, G., Magnesium ion mobility in post-spinels accessible at ambient pressure. *Chemical Communications* **2017**, 53 (37), 5171-5174.
38. Dompablo, M. E. A.-d.; Krich, C.; Nava-Avenidaño, J.; Biskup, N.; Palacin, M. R.; Bardé, F., A joint computational and experimental evaluation of CaMn_2O_4 polymorphs as cathode materials for Ca ion batteries. *Chemistry of Materials* **2016**, 28 (19), 6886-6893.
39. Lu, W.; Wang, J.; Sai Gautam, G.; Canepa, P., Searching Ternary Oxides and Chalcogenides as Positive Electrodes for Calcium Batteries. *Chemistry of Materials* **2021**, 33 (14), 5809-5821.
40. Yamaura, K.; Huang, Q.; Zhang, L.; Takada, K.; Baba, Y.; Nagai, T.; Matsui, Y.; Kosuda, K.; Takayama-Muromachi, E., Spinel-to- CaFe_2O_4 -Type Structural Transformation in LiMn_2O_4 under High Pressure. *Journal of the American Chemical Society* **2006**, 128 (29), 9448-9456.
41. Akimoto, J.; Awaka, J.; Kijima, N.; Takahashi, Y.; Maruta, Y.; Tokiwa, K.; Watanabe, T., High-pressure synthesis and crystal structure analysis of NaMn_2O_4 with the calcium ferrite-type structure. *Journal of Solid State Chemistry* **2006**, 179 (1), 169-174.
42. Yamaura, K.; Arai, M.; Sato, A.; Karki, A.; Young, D.; Movshovich, R.; Okamoto, S.; Mandrus, D.; Takayama-Muromachi, E., NaV_2O_4 : a quasi-1D metallic antiferromagnet with half-metallic chains. *Physical review letters* **2007**, 99 (19), 196601.
43. Hancock, J. C.; Griffith, K. J.; Choi, Y.; Bartel, C. J.; Lapidus, S. H.; Vaughey, J. T.; Ceder, G.; Poeppelmeier, K. R., Expanding the Ambient-Pressure Phase Space of CaFe_2O_4 -Type Sodium Postspinel Host-Guest Compounds. *ACS Organic & Inorganic Au* **2022**, 2 (1), 8-22.
44. G. Bruce, P.; Robert Armstrong, A.; L. Gitzendanner, R., New intercalation compounds for lithium batteries: layered LiMnO_2 . *Journal of Materials Chemistry* **1999**, 9 (1), 193-198.
45. Chiring, A.; Senguttuvan, P., Chemical pressure-stabilized post spinel- NaMnSnO_4 as potential cathode for sodium-ion batteries. *Bulletin of Materials Science* **2020**, 43 (1), 1-6.
46. Toby, B. H.; Von Dreele, R. B., GSAS-II: the genesis of a modern open-source all purpose crystallography software package. *Journal of Applied Crystallography* **2013**, 46 (2), 544-549.
47. Borkiewicz, O. J.; Shyam, B.; Wiaderek, K. M.; Kurtz, C.; Chupas, P. J.; Chapman, K. W., The AMPIX electrochemical cell: a versatile apparatus for in situ X-ray scattering and spectroscopic measurements. *Journal of Applied Crystallography* **2012**, 45 (6), 1261-1269.
48. Kresse, G.; Hafner, J., Norm-conserving and ultrasoft pseudopotentials for first-row and transition elements. *Journal of Physics: Condensed Matter* **1994**, 6 (40), 8245.
49. Blöchl, P. E.; Jepsen, O.; Andersen, O. K., Improved tetrahedron method for Brillouin-zone integrations. *Physical Review B* **1994**, 49 (23), 16223.
50. Perdew, J. P.; Burke, K.; Ernzerhof, M., Generalized gradient approximation made simple. *Physical review letters* **1996**, 77 (18), 3865.
51. Jain, A.; Ong, S. P.; Hautier, G.; Chen, W.; Richards, W. D.; Dacek, S.; Cholia, S.; Gunter, D.; Skinner, D.; Ceder, G., Commentary: The Materials Project: A materials genome approach to accelerating materials innovation. *APL materials* **2013**, 1 (1), 011002.
52. Jain, A.; Hautier, G.; Ong, S. P.; Moore, C. J.; Fischer, C. C.; Persson, K. A.; Ceder, G., Formation enthalpies by mixing GGA and GGA+U calculations. *Physical Review B* **2011**, 84 (4), 045115.
53. Henkelman, G.; Jónsson, H., Improved tangent estimate in the nudged elastic band method for finding minimum energy paths and saddle points. *The Journal of Chemical Physics* **2000**, 113 (22), 9978-9985.

54. Ong, S. P.; Richards, W. D.; Jain, A.; Hautier, G.; Kocher, M.; Cholia, S.; Gunter, D.; Chevrier, V. L.; Persson, K. A.; Ceder, G., Python Materials Genomics (pymatgen): A robust, open-source python library for materials analysis. *Computational Materials Science* **2013**, *68*, 314-319.
55. Klemm, W.; Beyersdorfer, K.; Oryschkewitsch, J., Über binäre Systeme aus Halogeniden II): Das Verhalten von NaCl, KCl, RbCl, NaI und KI zu den entsprechenden Magnesiumhalogeniden. *Zeitschrift für anorganische Chemie* **1948**, *256* (1-3), 25-36.
56. Jayaprakash, N.; Kalaiselvi, N.; Sun, Y. K., Combustion synthesized LiMnSnO₄ cathode for lithium batteries. *Electrochemistry Communications* **2008**, *10* (3), 455-460.
57. Amigues, A.; Glass, H.; Dutton, S., LiMnTiO₄ with the Na_{0.44}MnO₂ structure as a positive electrode for lithium-ion batteries. *Journal of The Electrochemical Society* **2015**, *163* (3), A396.
58. Kanamura, K.; Naito, H.; Yao, T.; Takehara, Z.-i., Structural change of the LiMn₂O₄ spinel structure induced by extraction of lithium. *Journal of Materials Chemistry* **1996**, *6* (1), 33-36.
59. Kuhn, A.; Martín, M.; García-Alvarado, F., New ramsdellites LiTi_{2-y}V_yO₄ (0 ≤ y ≤ 1): Synthesis, structure, magnetic properties and electrochemical performances as electrode materials for lithium batteries. *Journal of Solid State Chemistry* **2010**, *183* (1), 20-26.
60. Kuhn, A.; Martín, M.; García-Alvarado, F., Synthesis, Structure and Electrochemical Lithium Intercalation Chemistry of Ramsdellite-Type LiCrTiO₄. *Zeitschrift für anorganische und allgemeine Chemie* **2008**, *634* (5), 880-886.
61. Mikhailova, D.; Karakulina, O. M.; Batuk, D.; Hadermann, J.; Abakumov, A. M.; Herklotz, M.; Tsirlin, A. A.; Oswald, S.; Giebeler, L.; Schmidt, M.; Eckert, J.; Knapp, M.; Ehrenberg, H., Layered-to-Tunnel Structure Transformation and Oxygen Redox Chemistry in LiRhO₂ upon Li Extraction and Insertion. *Inorg. Chem.* **2016**, *55* (14), 7079-7089.
62. Mikhailova, D.; Maletti, S.; Missyul, A.; Büchner, B., Comparison of Layered Li(Li_{0.2}Rh_{0.8})O₂ and LiRhO₂ upon Li Removal: Stabilizing Effect of Li Substitution. *Inorg. Chem.* **2020**, *59* (13), 9108-9115.
63. Gu, Y.; Taniguchi, K.; Tajima, R.; Nishimura, S.-i.; Hashizume, D.; Yamada, A.; Takagi, H., A new “zero-strain” material for electrochemical lithium insertion. *Journal of Materials Chemistry A* **2013**, *1* (22), 6550-6552.
64. Chamorro, J. R.; Zuo, J. L.; Basse, E. N.; Watkins, A. K.; Zhu, G.; Zohar, A.; Wyckoff, K. E.; Kinnibrugh, T. L.; Lapidus, S. H.; Stemmer, S.; Clément, R. J.; Wilson, S. D.; Seshadri, R., Soft-Chemical Synthesis, Structure Evolution, and Insulator-to-Metal Transition in Pyrochlore-like λ-RhO₂. *Chem. Mater.* **2024**, *36*, 3, 1547–1558.
65. Nakajima, M.; Yabuuchi, N., Lithium-Excess Cation-Disordered Rocksalt-Type Oxide with Nanoscale Phase Segregation: Li_{1.25}Nb_{0.25}V_{0.5}O₂. *Chemistry of Materials* **2017**, *29* (16), 6927-6935.
66. Qi, R.; Konuma, I.; Campéon, B. D. L.; Kaneda, Y.; Kondo, M.; Yabuuchi, N., Highly Graphitic Carbon Coating on Li_{1.25}Nb_{0.25}V_{0.5}O₂ Derived from a Precursor with a Perylene Core for High-Power Battery Applications. *Chemistry of Materials* **2022**, *34* (4), 1946-1955.

TOC Graphic

